Asymmetric spiral chimeras on a spheric surface of nonlocally coupled phase oscillators

Chol-Ung Choe,[1,*] Myong-Su Ho,[2] and Ryong-Son Kim[1]
[1]*Research Group for Nonlinear Dynamics, Department of Physics, University of Science, Unjong-District, Pyongyang, Democratic People's Republic of Korea*
[2]*Department of Mechanics, Kim Il Sung University, Daesong-District, Pyongyang, Democratic People's Republic of Korea*

(Received 20 November 2022; accepted 1 February 2023; published 21 February 2023)

The spiral chimera state shows a remarkable spatiotemporal pattern in a two-dimensional array of oscillators for which the coherent spiral arms coexist with incoherent cores. In this work, we report on an asymmetric spiral chimera having incoherent cores of different sizes on the spherical surface of identical phase oscillators with nonlocal coupling. This asymmetric spiral chimera exhibits a strongly symmetry-broken state in the sense that not only the coherent and incoherent domains coexist, but also their incoherent cores are nonidentical, although the underlying coupling structure is symmetric. On the basis of analyses along the Ott-Antonsen invariant manifold, the bifurcation conditions of asymmetric spiral chimeras are derived, which reveals that the asymmetric spiral chimera state emerges via a supercritical symmetry-breaking bifurcation from the symmetric spiral chimera. For the coupling function composed of two Legendre modes, rigorous stability analyses are carried out to present a complete stability diagram for different types of spiral chimeras, including the stationary symmetric and asymmetric spiral chimeras as well as breathing asymmetric spiral chimera. For the general coupling scheme the asymmetric spiral chimera occurs as a result of competition between the odd and even Legendre modes of the coupling function. Our theoretical findings are verified by using extensive numerical simulations of the model system.

DOI: 10.1103/PhysRevE.107.024212

I. INTRODUCTION

Systems of coupled oscillators have been studied for many years as a paradigmatic model for spontaneous collective order in the area of nonlinear science. In particular, the synchronization of oscillator networks has been a subject of continued interest in many contexts of physical, biological, chemical, and even social systems [1–5].

Recently, much attention has been paid to a hybrid collective behavior in which a population of identical oscillators could split into two parts, one group with synchronization and another group with desynchronization, under the symmetric coupling schemes. Such a fascinating and counterintuitive state was first discovered by Kuramoto and Battogtokh [6] and later called the chimera state [7]. As a symmetry-breaking phenomenon, the chimeras attracted great interest and are found in networks of coupled oscillators with different dimensions and topologies (see the review articles [8–13] and references therein).

A particularly remarkable chimera is the spiral chimera reported by Kuramoto and Shima [14,15], which occurs in two-dimensional arrays of nonlocally coupled oscillators and consists of a phase-randomized core of desynchronized oscillators surrounded by a spiral wave of synchronized oscillators. The typical spiral symmetry that appears in the usual spiral waves with a phase defect at the center is broken for the spiral chimeras in the sense that in an extended core region the dynamics is no longer synchronized [16]. Such spiral chimeras were found in different topologies of networks, including a plane [15,17–19] with open boundary conditions, a flat torus [20–23,25], and a spherical surface [24–28] with periodic boundary conditions. Experimentally, the spiral chimera state was observed in the chemical oscillator system [29,30]. The single-core spiral chimera appears on the unbounded plane of oscillators, while on the surface of a sphere and a flat torus the primary spiral chimera states are represented by the two-core and four-core spiral chimeras, respectively. In particular, the multicore spiral chimeras studied so far have a reflection-symmetry with the same shape and size of incoherent cores and little is known about the existence of asymmetric spiral chimera state. Recently, an asymmetric spiral chimera state having the moving incoherent cores of different shapes was observed in numerical simulations of nonlocally coupled phase oscillators on a flat torus [23].

In this paper, we report on an asymmetric spiral chimera state that has motionless incoherent cores of different sizes and study theoretically the driving mechanisms for the symmetry-broken state. This asymmetric spiral chimera state exhibits symmetry breaking with an extreme incongruity in the sense that not only the coherent and incoherent domains coexist but also their incoherent cores are nonidentical, although the underlying coupling structure is symmetric. To understand the origin and the nature of asymmetric spiral chimera, we consider nonlocally coupled phase oscillators located on the unit sphere. On the basis of Ott-Antonsen reduction theory [31,32], we reduce our model to a low-dimensional system and derive the bifurcation conditions for

*cholung-choe@star-co.net.kp

the asymmetric spiral chimera to occur. This reveals that the asymmetric spiral chimera state emerges from the symmetric spiral chimera via a symmetry-breaking bifurcation. In particular, for the nonlocal coupling function composed of two successive harmonic modes, we perform a rigorous stability analysis to present a complete stability diagram for different types of spiral chimeras, including the symmetric and asymmetric spiral chimeras as well as breathing asymmetric spiral chimera. We find that, for the general coupling scheme, the competition between the odd and even Legendre modes of the coupling functions incurs the asymmetric spiral chimeras. Our theoretical findings are verified by using extensive numerical simulations of the model system.

II. RESULTS

A. Governing equations

1. Model

We consider a two-dimensional array of nonlocally coupled identical phase oscillators on the surface of unit sphere $\mathbb{S}^2$ as follows:

$$\frac{\partial\psi(\mathbf{r},t)}{\partial t}=\omega+\int_{\mathbb{S}^2}G(\mathbf{r},\mathbf{r}')\sin[\psi(\mathbf{r}',t)-\psi(\mathbf{r},t)-\alpha]d\mathbf{r}', \tag{1}$$

where $\psi(\mathbf{r},t)$ is the phase of the oscillator at position $\mathbf{r}\in\mathbb{S}^2$ at time t, ω is the natural frequency, and α denotes the phase shift parameter. The identical frequency ω plays no role in the dynamics and we can set $\omega=0$ without loss of generality.

The kernel $G(\mathbf{r},\mathbf{r}')$ denotes the nonlocal coupling function, which represents the strength of interaction between oscillators and is assumed to depend only on the great circle distance $\gamma(\mathbf{r},\mathbf{r}')>0$ between two positions $\mathbf{r}$ and $\mathbf{r}'$ on the unit sphere $\mathbb{S}^2$. Then the function G can be expanded via the Legendre polynomials P_ℓ:

$$G(\cos\gamma)=\frac{1}{4\pi}\sum_{\ell=0}^{\infty}\kappa_\ell P_\ell(\cos\gamma),$$

where the coefficients are given by $\kappa_\ell=2\pi(2\ell+1)\int_{-1}^{1}G(x)P_\ell(x)dx$.

In this work, we consider the so-called *balanced* coupling with $\kappa_0=0$, which gives $\int_{\mathbb{S}^2}G(\mathbf{r},\mathbf{r}')d\mathbf{r}'=0$. Such a balanced coupling schemes exhibit both attracting and repulsive interactions depending on the distance between oscillators and are typical in neuroscience, referred to as the Mexican-hat-shaped coupling functions [33]. It is known that the zeroth coefficient κ_0 plays no role in the existence of spiral chimera states and there exists no fully synchronized state in the system (1) with the balanced coupling function [27]. Further, retaining the K terms in the Legendre series, we obtain the coupling function to be considered in this work as following:

$$G_K(\mathbf{r},\mathbf{r}')=\frac{1}{4\pi}\sum_{\ell=1}^{K}\kappa_\ell P_\ell(\cos\gamma). \tag{2}$$

Note that, without loss of generality, one of the coefficients κ_ℓ can be set to be a fixed value, e.g., $\kappa_1=1$, by the rescaling time in Eq. (1).

In particular, we focus on the coupling function containing only two nonvanishing coefficients κ_1 and κ_2, given by

$$G_2(\mathbf{r},\mathbf{r}')=\frac{1}{4\pi}\Big[\kappa_1\cos\gamma+\frac{\kappa_2}{2}(3\cos^2\gamma-1)\Big]. \tag{3}$$

For the coupling function (3), we can perform the stability analysis, which allows us to compute the complete bifurcation diagram for asymmetric spiral chimeras, as shown in Fig. 1. We note that the coupling function G_2 was considered in Ref. [27] in the context of pure symmetric spiral chimera states.

2. System reduction

We define a complex order parameter $Z(\mathbf{r},t)\equiv R(\mathbf{r},t)e^{i\Psi(\mathbf{r},t)}$ that describes a macroscopic behavior of oscillators as

$$Z(\mathbf{r},t)=e^{-i\alpha}\int_{\mathbb{S}^2}G(\mathbf{r},\mathbf{r}')e^{i\psi(\mathbf{r}',t)}d\mathbf{r}'. \tag{4}$$

The macroscopic state of the phase oscillator system (1) can be described by a distribution function $f(\psi,\mathbf{r},t)$ representing the probability density that the oscillator at position $\mathbf{r}$ has the phase ψ at time t. Following the Ott-Antonsen ansatz theory [31,32], the asymptotic evolution of the distribution function f is described by a low-dimensional system for a complex-valued function $z(\mathbf{r},t)$ as follows:

$$\frac{\partial z(\mathbf{r},t)}{\partial t}=i\omega z+\frac{1}{2}(Z-z^2Z^*), \tag{5a}$$

$$Z(\mathbf{r},t)=e^{-i\alpha}\int_{\mathbb{S}^2}G(\mathbf{r},\mathbf{r}')z(\mathbf{r}',t)d\mathbf{r}', \tag{5b}$$

where the asterisk denotes complex conjugate. We call $z(\mathbf{r},t)$ the local order parameter.

The derivations of Eq. (5) were performed in a number of previous studies [17,20,26,27] and we refer the interested reader to those papers. Note that only the local order parameters that satisfy $|z(\mathbf{r},t)|\leqslant 1$ are physically meaningful and that the oscillators corresponding to $|z(\mathbf{r},t)|=1$ and $|z(\mathbf{r},t)|<1$ indicate the coherent and incoherent ones, respectively.

B. Main results

1. Stability diagram

The results of analyzing the reduced Eq. (5) for the coupling function given by Eq. (3) are summarized in Fig. 1, which shows a bifurcation diagram for different types of spiral chimera states in the $[\alpha,\kappa(\equiv\kappa_2)]$ plane. We found stability regions for different types of spiral chimeras. (i) Symmetric two-core spiral chimera (red), which consists of two incoherent cores surrounded by coherent spiral arms, having a reflection symmetry. (ii) Symmetric striped (light pink), which has two incoherent cores as well as an incoherent stripe with reflection symmetry. (iii) Asymmetric two-core spiral (cyan) and (iv) asymmetric striped spiral (green) chimeras, corresponding to the symmetry-broken versions of the two-core and striped spiral chimeras, respectively.

The transition from the symmetric two-core spiral chimera to the asymmetric one occurs on the boundary S_1, which is analytically determined by Eq. (25). The curve S_2 indicates

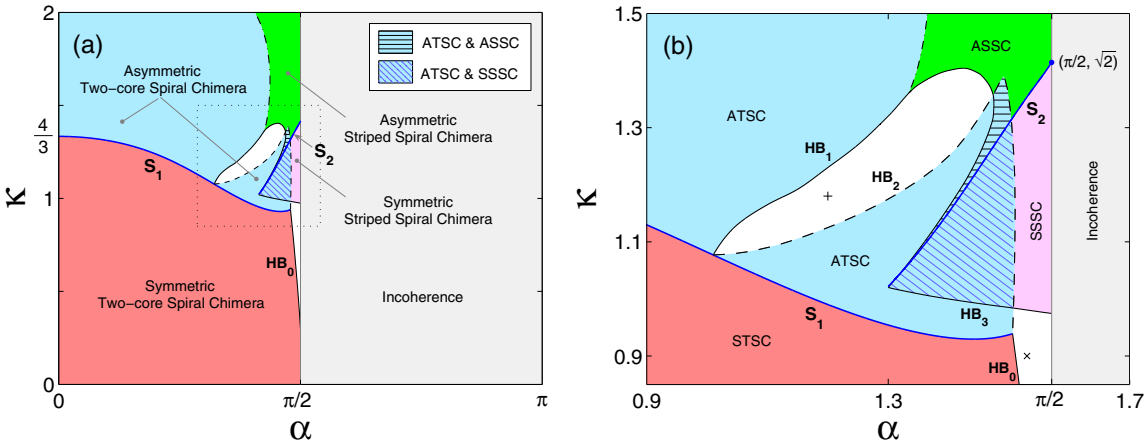

FIG. 1. (a) Stability diagram for the reduced Eq. (5) with the coupling function (3), where $\kappa_1 = 1$ and $\kappa \equiv \kappa_2$. Symmetric two-core spiral chimera (STSC) and asymmetric one (ATSC) occur in the red and cyan parameter regions, respectively, and the transition boundary S_1 between them is determined by Eq. (25). Transition boundary S_2 between the symmetric striped spiral chimera (SSSC) and asymmetric one (ASSC), shown in the light pink and green regions, respectively, is given by Eq. (28). Hatched regions indicate the bistable regime where different spiral chimeras coexist. (b) Enlargement of rectangular part in panel (a). Stability boundaries labeled HB_1, HB_2, and HB_3 denote the Hopf bifurcation curves, determined by solving the characteristic Eq. (33) (see Figs. 9–11). The signs + and × indicate parameter locations for the spiral chimera patterns displayed in Figs. 4 and 5, respectively.

the transition boundary between the symmetric striped spiral chimera and the asymmetric one. The symmetry-breaking bifurcation analyses occurring on the boundaries S_1 and S_2 are considered in Sec. III.

The asymmetric spiral chimera states undergo destabilization via Hopf bifurcation on the boundaries marked HB_1 (solid line) and HB_2 (dashed line). All the Hopf bifurcation curves in Fig. 1(b), labeled HB_1, HB_2, and HB_3, are determined via the stability analysis of chimera states in Sec. IV. The parameter region for the incoherent state (gray-colored) and the stability boundary HB_0 were obtained, based on the results found in Ref. [27].

2. *Numerical simulations*

The numerical simulations were carried out by integrating the discretized version of Eqs. (1) and (3) for the number of oscillators equal to $N = 5000$ using the fourth-order Runge-Kutta method with a time step of 0.02.

Figures 2(a) and 2(b) show the (i) symmetric two-core spiral chimera and (ii) symmetric striped spiral chimera states, respectively, observed in direct numerical simulations. The upper panels of Fig. 2 depict the snapshots of phase distributions $\psi(\mathbf{r})$ on the sphere and their two-dimensional projections viewed from above and below. We can observe that the sizes of incoherent cores located around the north and south poles are equal and the phase patterns have a reflection symmetry about the equator.

In the lower panels of Fig. 2, the longitudinal profiles $R(\theta)$ of the order parameter and the corresponding Δ values are displayed, where the open circles correspond to the results from direct numerical simulations of Eq. (1). Numerically, the order parameter was quantified by Eq. (4), while the Δ value was evaluated by the phase velocity of oscillators in the coherent domain. The gray boxes in the lower panels of Fig. 2 denote the incoherent domain, which shows clearly the identical radii of the north and south incoherent cores $r_N = r_S$.

Figure 3 depicts the typical examples of *asymmetric* spiral chimera states (iii) and (iv), obtained by direct numerical simulations of Eq. (1) for the coupling function (3). We can see clearly that the phase snapshots and the corresponding longitudinal profiles exhibit asymmetries with respect to the equatorial plane defined by $\theta = \pi/2$.

In the parameter region enclosed with Hopf boundaries HB_1 and HB_2 in Fig. 1(b), both the symmetric and asymmetric spiral chimera states are unstable. Simulating the system in that parameter region, we observe a *breathing* asymmetric spiral chimera state. An example of a breathing asymmetric spiral chimera is depicted in Fig. 4 for which the parameter values correspond to the plus sign in Fig. 1(b). Figure 4(a) illustrates a series of phase snapshots during a breathing period. We can see in Fig. 4(b) that the maximum value (blue solid line) in the spatial distribution of $R(\mathbf{r}, t)$ presents a periodic oscillation around the theoretically obtained steady solution (gray dashed line).

Figure 5 shows another symmetry-breaking state, the so-called near-incoherent chimera, observed in the numerical simulations for parameter values corresponding to the multiplication sign in Fig. 1(b).

III. SYMMETRY-BREAKING BIFURCATIONS

A. Self-consistency equation

Many dynamical regimes of interest, observed in Eq. (5), are stationary in a rotating coordinate frame with a (yet unknown) collective frequency Ω. Under the transformation given by $z \to ze^{i\Omega t}$ and $Z \to Ze^{i\Omega t}$, Eq. (5) is replaced by

$$\frac{\partial z(\mathbf{r}, t)}{\partial t} = i\Delta z + \frac{1}{2}(Z - z^2 Z^*), \tag{6a}$$

$$Z(\mathbf{r}, t) = e^{-i\alpha} \int_{\mathbb{S}^2} G(\mathbf{r}, \mathbf{r}') z(\mathbf{r}', t) d\mathbf{r}', \tag{6b}$$

where $\Delta \equiv \omega - \Omega$.

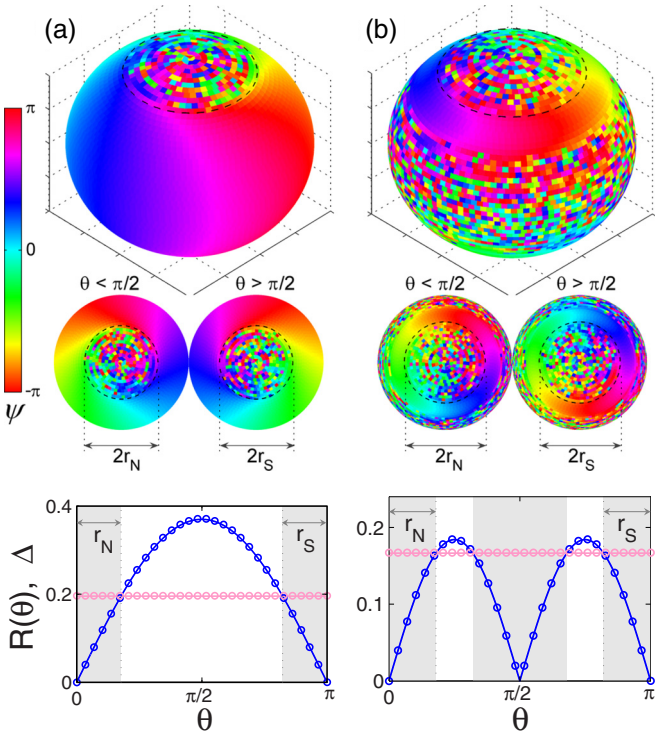

FIG. 2. Symmetric spiral chimera patterns. (a) Symmetric two-core spiral chimera state for parameter values $(\alpha, \kappa_1, \kappa_2) = (0.7, 1, 1)$. (b) Symmetric striped spiral chimera for $(\alpha, \kappa_1, \kappa_2) = (1.43, 1, 1.1)$. The upper panels display the phase snapshots on sphere and the two-dimensional projections viewed from the north and south poles, obtained by numerical simulations of Eqs. (1) and (3) for the number of oscillators equal to $N = 5000$. The lower panels show the longitudinal profiles (blue) of order parameter Z and the Δ value (red), where open circles represent results from numerical simulations while solid lines correspond to theoretically obtained results. Gray boxes denote the incoherent domains of which the outer parts present identical radii of incoherent cores $r_N = r_S$.

The stationary spatial profile of the rotating waves is represented by the fixed point of Eq. (6a)

$$z_0(\mathbf{r}) = ih(\mathbf{r})Z(\mathbf{r}), \tag{7}$$

where $h(\mathbf{r}) = \frac{1}{\Delta + \sqrt{\Delta^2 - R^2(\mathbf{r})}}$ with the square-root notation $\sqrt{d} = \sqrt{|d|}e^{i\arg(d)/2}$. Below, such a square root notation will be used for other quantities as well. Inserting Eq. (7) into Eq. (6b), we obtain the self-consistency equation for $Z(\mathbf{r}) \equiv R(\mathbf{r})e^{i\Psi(\mathbf{r})}$ as

$$Z(\mathbf{r}) = e^{i\beta} \int_{\mathbb{S}^2} G(\mathbf{r}, \mathbf{r}')h(\mathbf{r}')Z(\mathbf{r}')d\mathbf{r}', \tag{8}$$

where $\beta = \frac{\pi}{2} - \alpha$.

Since the function h depends on $|Z|$, Eq. (8) can be considered as a nonlinear eigenvalue problem for the complex eigenfunction $Z(\mathbf{r})$ and the real eigenvalue Δ. Unlike the linear eigenvalue problem, the eigenfunction Z has no arbitrariness in its real multiples. Instead Z is only determined up to an arbitrary rotation since Eq. (8) is invariant under any rigid rotation $Z(\mathbf{r}) \to Z(\mathbf{r})e^{i\Psi_0}$. Therefore, we are free to specify the value of $\arg[Z(\mathbf{r})] \equiv \Psi(\mathbf{r})$ at a chosen point by an arbitrary value that we want. This provides an additional condition to determine Δ and $Z(\mathbf{r})$ in a closed form, as will be shown below.

We note that Eq. (8) has a trivial solution $Z(\mathbf{r}) = 0$ for any kernel $G(\mathbf{r}, \mathbf{r}')$, which represents the completely incoherent state. Taking into account the equality $\int_{\mathbb{S}^2} G(\mathbf{r}, \mathbf{r}')d\mathbf{r}' = 0$ for the balanced coupling, one can see that Eq. (8) never allows for a nonzero constant solution. Therefore, the fully synchronized state given by $Z(\mathbf{r}) = \text{const.} \neq 0$ could not occur for the balanced coupling.

B. Reduced self-consistency

In the spherical polar coordinates with the azimuthal angle $\phi \in [0, 2\pi)$ and the polar angle $\theta \in [0, \pi]$, we use the spherical harmonic addition theorem $P_\ell(\cos\gamma) = \frac{4\pi}{2\ell+1}\sum_{m=-\ell}^{\ell} Y_\ell^m(\theta, \phi)[Y_\ell^m(\theta', \phi')]^*$ to expand the coupling kernel (2) as follows:

$$G(\mathbf{r}, \mathbf{r}') = \sum_{\ell=1}^{K} \frac{\kappa_\ell}{2\ell+1} \sum_{m=-\ell}^{\ell} Y_\ell^m(\mathbf{r})\big[Y_\ell^m(\mathbf{r}')\big]^*, \tag{9}$$

where $Y_\ell^m(\mathbf{r})$ is the complex-valued spherical harmonics of degree $\ell \geqslant 1$ and order $|m| \leqslant \ell$, given by $Y_\ell^m(\theta, \phi) = (-1)^m\sqrt{\frac{(2\ell+1)}{4\pi}\frac{(\ell-m)!}{(\ell+m)!}}P_\ell^m(\cos\theta)e^{im\phi}$ with the associated Legendre polynomials P_ℓ^m.

Considering the appearance of the phase patterns in Figs. 2 and 3, we look for solutions of Eq. (8) in a spiral wave form of $R(\mathbf{r}) = R(\theta)$ and $\Psi(\mathbf{r}) = \Theta(\theta) + \phi$, i.e.,

$$Z(\mathbf{r}) = \hat{Z}(\theta)e^{i\phi} = R(\theta)e^{i[\Theta(\theta)+\phi]}.$$

Substituting Eq. (9) into Eq. (8) and integrating it with respect to ϕ' yield

$$Z = e^{i\phi}\sum_{\ell=1}^{K} a_\ell P_\ell^1(\cos\theta), \tag{10}$$

where

$$a_\ell = \frac{\kappa_\ell e^{i\beta}}{2\ell(\ell+1)}\int_0^\pi h(\theta')P_\ell^1(\cos\theta')\hat{Z}(\theta')\sin\theta' d\theta'. \tag{11}$$

Plugging Eq. (10) into Eq. (11), we obtain the reduced self-consistency equation for a_ℓ as follows:

$$a_\ell = \frac{\kappa_\ell e^{i\beta}}{\ell(\ell+1)}\sum_{k=1}^{K} a_k\big\langle\tilde{h}(x)P_k^1(x)P_\ell^1(x)\big\rangle, \tag{12}$$

where $\tilde{h}(x) = \frac{1}{\Delta + \sqrt{\Delta^2 - |\sum_{n=1}^{K} a_n P_n^1(x)|^2}}$ and the angular bracket denotes a spatial average defined by $\langle f\rangle \equiv \frac{1}{2}\int_{-1}^{1} f(x)dx$.

Since the function $\tilde{h}$ involves unknown quantities a_ℓ and Δ, the number of unknowns seems to be larger than that of equations: we have to solve the K complex Eq. (12) for the $K+1$ unknowns $a_\ell \in \mathbb{C}$ and $\Delta \in \mathbb{R}$. By using the arbitrariness of choice of $\arg(Z) \equiv \Psi_0$, one of the K complex quantities a_ℓ can be set to be real without loss of generality. This makes it possible to determine all the unknowns in terms of parameters κ_ℓ and β in a closed form.

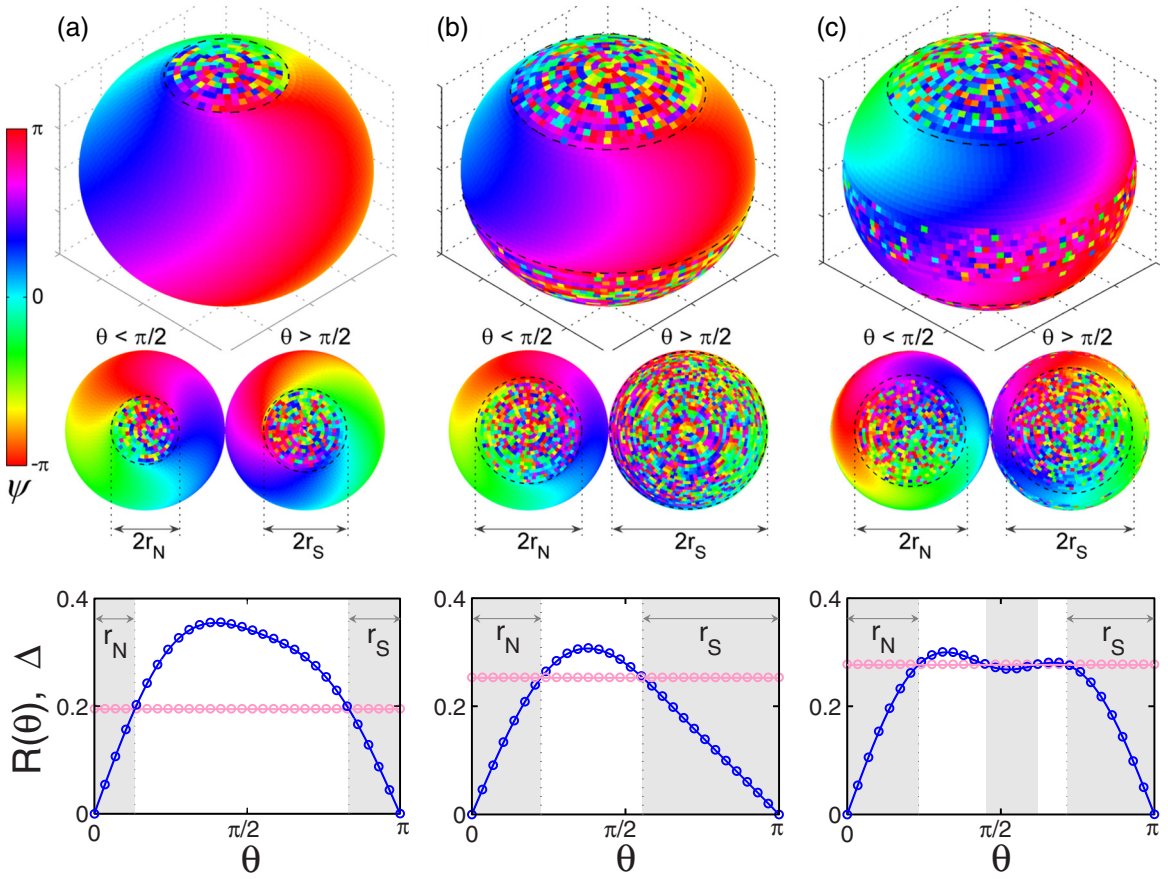

FIG. 3. Asymmetric spiral chimera patterns in the same format as Fig. 2. (a,b) Asymmetric two-core spiral chimera states, corresponding to parameter values $(\alpha, \kappa_1, \kappa_2) = (0.7, 1, 1.35)$ and $(\alpha, \kappa) = (1.2, 1, 1.06)$, respectively. (c) Asymmetric striped spiral chimera for $(\alpha, \kappa_1, \kappa_2) = (1.43, 1, 1.46)$. Inequality of incoherent core radii $r_N \neq r_S$ features the asymmetry of phase patterns and longitudinal profiles.

C. Explicit solutions

For the coupling function G_2 given by Eq. (3), analytical solutions of the self-consistency Eq. (8) can be found. Equations (10) and (12) for $K = 2$ can be written by

$$R(\theta)e^{i\Psi(\theta,\phi)} = (a + b\cos\theta)\sin\theta e^{i\phi}, \tag{13}$$

and

$$a = \frac{\kappa_1 e^{i\beta}}{2}\langle(1-x^2)(a+bx)\tilde{h}\rangle, \tag{14a}$$

$$b = \frac{3\kappa_2 e^{i\beta}}{2}\langle x(1-x^2)(a+bx)\tilde{h}\rangle, \tag{14b}$$

where $a = a_1$, $b = 3a_2$, and $\tilde{h} = \frac{1}{\Delta+\sqrt{\Delta^2-(1-x^2)|a+bx|^2}}$.

1. *Symmetric two-core spiral chimera*

We can see that Eq. (14b) has a solution $b = 0$ since the integrand in the right-hand side becomes an odd function. Then the order parameter (13) reduces to

$$Z_1(\mathbf{r}) = a\sin\theta e^{i\phi}, \tag{15}$$

which corresponds to the symmetric two-core spiral chimera state, studied in Refs. [24,26,27]. Note that, without loss of generality, a can be assumed to be real by defining $\arg(Z_1) = 0$ at $\phi = 0$. Two real values a and Δ are determined from Eq. (14a), which can be written by

$$2a^2 = \kappa_1 e^{i\beta}\langle\Delta - \sqrt{\Delta^2 - a^2(1-x^2)}\rangle. \tag{16}$$

In the lower panel of Fig. 2(a), the solid lines represent the results for $R(\theta) \equiv a\sin\theta$ and Δ, obtained by solving Eq. (16) for parameter values $\alpha = 0.7$ and $\kappa_1 = 1$.

The size of the incoherent cores in the spiral chimeras can be measured by the great circle arc length between the center of the core and the coherence-incoherence boundary, which we call the radius of the incoherent cores. The coherence-incoherence boundary is determined by the intersection of two lines $R(\theta)$ and Δ, as depicted in Fig. 2. Thus the radii of the north and south cores for the symmetric two-core spiral chimera state are given by

$$r_N = r_S = \arcsin\left(\frac{\Delta}{a}\right).$$

Defining $\bar{a} = a/\kappa_1$ and $\bar{\Delta} = \Delta/\kappa_1$, Eq. (16) can be written by

$$2\bar{a}^2 = e^{i\beta}\langle\bar{\Delta} - \sqrt{\bar{\Delta}^2 - \bar{a}^2(1-x^2)}\rangle. \tag{17}$$

The solutions of Eq. (17), $\bar{a}$ and $\bar{\Delta}$, depend only on the parameter β, or equivalently, α. It follows that both a and Δ are proportional to κ_1 and thus the radii r_N and r_S of symmetrical two-core spiral chimeras depend only on α, irrespective of κ_1 as well as κ_2.

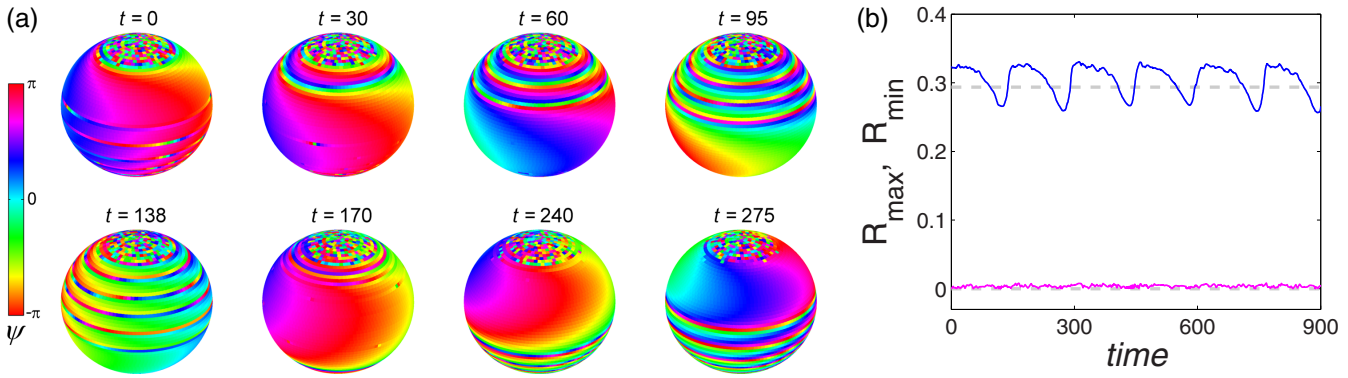

FIG. 4. Breathing asymmetric spiral chimera state, observed in numerical simulations of Eqs. (1) and (3). (a) A series of phase snapshots for a time period $T = 275s$. (b) Time dynamics of the maximum (blue) and minimum (red) values over the spherical surface of $R(\mathbf{r}, t)$. Dashed (gray) lines indicate theoretical values of $R_{\max}$ and $R_{\min}$ for the unstable steady state, determined by Eqs. (13) and (14). Parameters: $\alpha = 1.2$, $\kappa_1 = 1$, and $\kappa_2 = 1.18$, which correspond to the plus sign shown in Fig. 1(b).

2. *Symmetric striped spiral chimera*

It is obvious that Eq. (14a) allows a solution $a = 0$ and then Eq. (13) becomes

$$Z_2(\mathbf{r}) = b \sin\theta \cos\theta e^{i\phi}. \tag{18}$$

The order parameter (18) represents the striped spiral chimera state, which was investigated in Ref. [27]. Defining $\arg(Z_2) = 0$ at $\phi = 0$, we can set b to be real. Two real values b and Δ are determined by solving Eq. (14b), i.e., the following complex equation:

$$2b^2 = 3\kappa_2 e^{i\beta}\langle \Delta - \sqrt{\Delta^2 - b^2x^2(1-x^2)}\rangle. \tag{19}$$

The graph of $R(\theta) \equiv b \sin\theta|\cos\theta|$ and the corresponding value of Δ, determined by solving Eq. (19) for $\alpha = 1.43$ and $\kappa_2 = 1.1$, are depicted by solid lines in the lower panel of Fig. 2(b). The radii of two cores for the symmetric striped spiral chimera, described by Eq. (18), are determined by

$$r_N = r_S = \frac{1}{2}\arcsin\left(\frac{2\Delta}{b}\right).$$

Defining $\hat{b} = b/\kappa_2$ and $\hat{\Delta} = \Delta/\kappa_2$, Eq. (19) becomes

$$2\hat{b}^2 = 3e^{i\beta}\langle \hat{\Delta} - \sqrt{\hat{\Delta}^2 - \hat{b}^2x^2(1-x^2)}\rangle, \tag{20}$$

which does not contain the parameter κ_2. This means that both b and Δ are proportional to κ_2 and thus the radii r_N and r_S do not depend on κ_2. We note that the parameter κ_1 has no effect on the symmetrical striped spiral chimera and thus the incoherent core radius is independent of κ_1 as well.

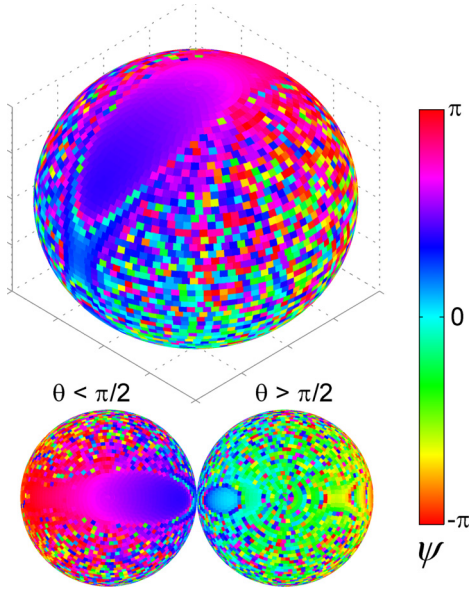

FIG. 5. Phase snapshot of near-incoherent asymmetric chimera state. Parameter values: $\alpha = 1.53$, $\kappa_1 = 1$, and $\kappa_2 = 0.9$, corresponding to the multiplication sign shown in Fig. 1(b).

3. *Asymmetric spiral chimera*

We note that both the two-core and striped spiral chimeras, represented, respectively, by Eqs. (15) and (18), have the *reflection symmetry* about the equator.

However, when both a and b are nonzero, the order parameter given by Eq. (13) describes a spiral chimera pattern which has an *asymmetry* with respect to the equator. One can set $a \in \mathbb{R}$ and $b \in \mathbb{C}$ by defining $\arg(Z_3) = 0$ at $\theta = \pi/2$ and $\phi = 0$. Thus the complex Eq. (14) is equivalent to four real equations for the four real unknowns a, b_R, b_I, and Δ. The solutions, if they exist, are to be expressed in terms of parameters κ_1, κ_2, and β. We note that, taking into account the arbitrariness of $\arg(Z)$, either of the two coefficients a and b can be assumed to be real.

In the lower panels of Fig. 3, the solid curves indicate the longitudinal profiles of asymmetric spiral chimeras given by

$$R(\theta) \equiv \sin\theta|a + b\cos\theta|,$$

for which a and b are obtained by solving Eq. (14). These theoretical solutions agree very well with the result from the direct numerical simulations of the model system (1) with the kernel (3), as marked by the open circles. We observe that there is a distinct difference in the size of the north and south cores $r_N \neq r_S$ for the asymmetric spiral chimera state.

Given the values of a, b, and Δ as solutions of Eq. (14), we can determine the local order parameter $z_0(\mathbf{r})$ through Eqs. (7) and (13). Figure 6 illustrates typical snapshots of

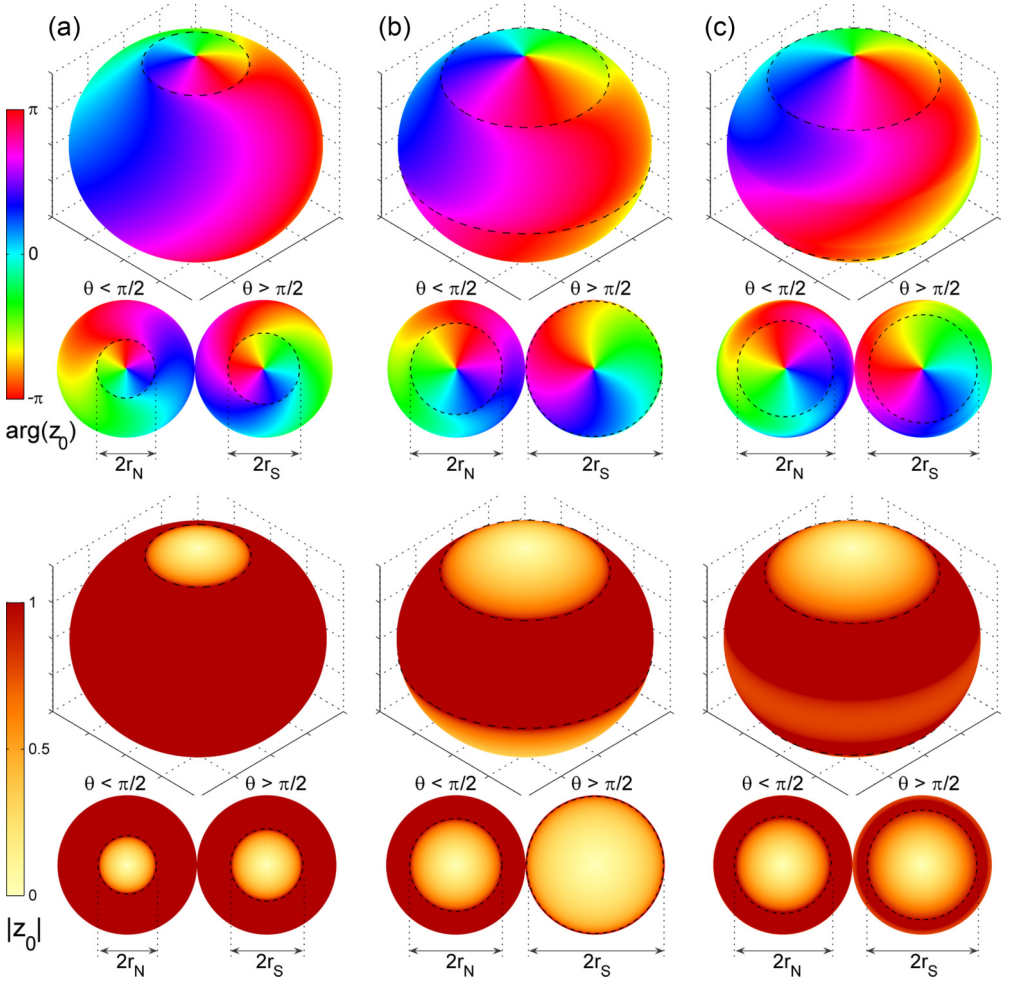

FIG. 6. Asymmetric spiral chimera patterns represented by local order parameter $z_0(\mathbf{r})$, determined by solving Eqs. (7), (14), and (13). Upper and lower rows indicate the snapshots for the phase and modulus of $z_0(\mathbf{r})$, respectively. Parameter values of panels (a), (b), and (c) are the same as Figs. 3(a), 3(b), and 3(c), respectively.

$\arg(z_0)$ and $|z_0|$ for the parameter values used in Fig. 3. Compared to Fig. 3, we observe that, as a theoretical prediction for the asymmetric spiral chimera state, the phase pattern of $z_0(\mathbf{r})$ is well consistent with the result from the direct simulations of Eq. (1). In the lower panels of Fig. 6, we see that the coherent and incoherent domains, represented by $|z_0(\mathbf{r})| = 1$ and $|z_0(\mathbf{r})| < 1$, respectively, are clearly distinguished.

D. Symmetry-breaking bifurcation

1. Numerical continuation

The incoherent core radii of the asymmetric spiral chimera in the north and south poles are determined by

$$r_N = \min(\theta_0), \quad r_S = \pi - \max(\theta_0), \tag{21}$$

where $\theta_0 \in [0, \pi]$ denotes the roots of the following equation:

$$|a + b\cos\theta_0| \sin\theta_0 = \Delta. \tag{22}$$

We performed numerical continuations of solving Eqs. (14) and (22) for the varying κ to see how the symmetry breaking in the size of the north and south incoherent cores occurs. Figure 7 shows the radii r_N and r_S as a function of κ for fixed values of α, where the lines represent the result obtained by the numerical continuation of Eq. (21). Figures 7(a) and 7(b) correspond to the α values for the two-core spiral chimeras while Fig. 7(c) concerns the striped spiral chimera state.

According to our numerical continuations, as κ decreases, the two asymmetric solution branches ($r_N \neq r_S$) meet at a bifurcation point, as marked by $S_{1,2}$ in Fig. 7, and then merge into the symmetric solutions ($r_N = r_S$). With the increase of κ, the symmetric solutions that exist prior to the bifurcation continue as symmetric solutions after the bifurcation, which implies the coexistence of the symmetric and asymmetric solution branches. In Fig. 7, the solid and dashed lines denote the stable and unstable states, respectively, which is validated by the stability analysis of Sec. IV (cf. Figs. 8–10). As a result, a supercritical symmetry-breaking bifurcation occurs at the bifurcation points $S_{1,2}$.

The open circles seen in Fig. 7 correspond to the result from the direct numerical simulation of model system (1) with the kernel (3), which are in good agreement with those obtained by the numerical continuation.

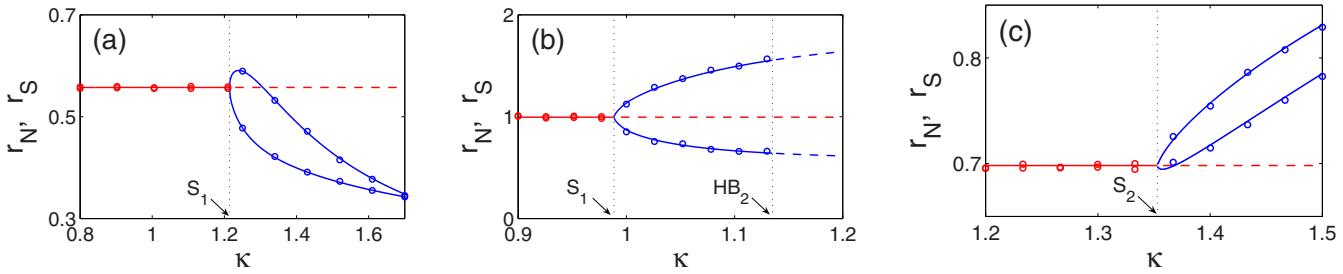

FIG. 7. Bifurcation diagrams of incoherent core radii in the north and south poles r_N and r_S, as $\kappa(\equiv\kappa_2)$ is varied. Asymmetric spiral chimeras occur via the symmetry-breaking bifurcation at the boundaries $S_{1,2}$. Symmetric ($r_N = r_S$) and asymmetric ($r_N \neq r_S$) branches, marked by red and blue lines, respectively, are all determined by solving Eqs. (14), (21), and (22). Solid and dashed lines correspond to stable and unstable states, respectively, as identified by the stability analysis of Sec. IV (see Figs. 8–10). Open circles denote results, obtained by direct numerical simulation of Eqs. (1) and (3). Parameters: $\kappa_1 = 1$, (a) $\alpha = 0.7$, (b) $\alpha = 1.2$, and (c) $\alpha = 1.53$.

2. *Transition to asymmetric two-core spiral chimera*

Now we seek conditions for the asymmetric branch of solutions to bifurcate off the symmetric two-core spiral chimera state. The incipient occurrence of the asymmetric two-core spiral chimera can be viewed by letting $|b| \to 0$ in Eq. (14) for $a \in \mathbb{R}$ and $b \in \mathbb{C}$.

We expand the function $\tilde{h}$ in a two-variable Taylor series for small b_R and b_I:

$$\tilde{h} = \tilde{h}_0(x;a) + \tilde{h}_1(x;a)b_R + \mathcal{O}(|b|^2),$$

where $\tilde{h}_0 = \frac{1}{\Delta+\sqrt{\Delta^2-a^2(1-x^2)}}$ and $\tilde{h}_1 = \frac{ax(1-x^2)\tilde{h}_0^2}{\sqrt{\Delta^2-a^2(1-x^2)}}$. Then Eq. (14) becomes

$$1 = \frac{\kappa_1 e^{i\beta}}{2}\langle(1-x^2)\tilde{h}_0\rangle + \mathcal{O}(|b|^2), \tag{23a}$$

$$b = \frac{3\kappa_2 e^{i\beta}}{2}\langle x(1-x^2)(bx\tilde{h}_0 + ab_R\tilde{h}_1)\rangle + \mathcal{O}(|b|^3). \tag{23b}$$

As $|b| \to 0$, Eq. (23a) recovers Eq. (16), or equivalently Eq. (17), which gives the values of $\bar{a}$ and $\bar{\Delta}$ that are independent of parameters κ_1 and κ_2. Then, in the first approximation, Eq. (23b) reduces to

$$\begin{pmatrix} \mu_R - \frac{\kappa_1}{\kappa_2} & -\nu_I \\ \mu_I & \nu_R - \frac{\kappa_1}{\kappa_2} \end{pmatrix}\begin{pmatrix} b_R \\ b_I \end{pmatrix} = 0, \tag{24}$$

where μ and ν are complex quantities given by

$$s\mu = \bar{\Delta}(3\bar{\Delta}A - 1)e^{i\beta}/2\bar{a}^2, \quad \nu = (\bar{\Delta} - 3B)e^{i\beta}/2\bar{a}^2,$$

with $A = \langle x^2/\sqrt{\bar{\Delta}^2 - \bar{a}^2(1-x^2)}\rangle$ and $B = \langle x^2\sqrt{\bar{\Delta}^2 - \bar{a}^2(1-x^2)}\rangle$. The definite integrals A and B can be calculated to yield $A = \frac{1}{2\bar{a}}[\frac{\bar{\Delta}}{\bar{a}} + (1-\frac{\bar{\Delta}^2}{\bar{a}^2})(\ln\sqrt{\frac{\bar{a}+\bar{\Delta}}{\bar{a}-\bar{\Delta}}} - \frac{i\pi}{2})]$ and $B = \frac{\bar{a}}{8}[\frac{\bar{\Delta}}{\bar{a}}(1+\frac{\bar{\Delta}^2}{\bar{a}^2}) - (1-\frac{\bar{\Delta}^2}{\bar{a}^2})^2(\ln\sqrt{\frac{\bar{a}+\bar{\Delta}}{\bar{a}-\bar{\Delta}}} - \frac{i\pi}{2})]$. We note that the quantities μ and ν describing the symmetric two-core spiral chimera state depend only on the parameter β, or equivalently, α, irrespective of κ_1 and κ_2.

The parameter location where the asymmetric solution branch bifurcates off the symmetric one can be revealed via the implicit function theorem: setting the coefficient determinant of Eq. (24) equal to zero gives the bifurcation condition as

$$\frac{\kappa_2}{\kappa_1} = f_1(\alpha) \equiv \frac{2}{(\mu+\nu)_R + \sqrt{(\mu-\nu)_R^2 - 4\mu_1\nu_I}}. \tag{25}$$

Solving numerically Eq. (17) for a fixed α and substituting the solutions into Eq. (25), we obtain the transition point from symmetric two-core spiral chimera to an asymmetric one.

In Fig. 1, the stability boundary S_1 was determined by Eq. (25). Separating Eq. (17) into the real and imaginary parts yields that $\bar{a} = \bar{\Delta} = 1/4$ at $\alpha = \frac{\pi}{2}$ while $\bar{\Delta} = 0$ and $\bar{a} = \frac{\pi}{8}$ at $\alpha = 0$. Thus we can find that $\kappa = \frac{4}{3}$ and $\kappa = 1$ for $\alpha = 0$ and $\alpha = \frac{\pi}{2}$, respectively, as shown in Fig. 1.

3. *Transition to asymmetric striped chimera*

Let us look for the transition point from the symmetric striped spiral chimera to the asymmetric one.

Now the values of a and b in Eq. (14) are assumed to be complex and real numbers, respectively. Expanding the function $\tilde{h}$ in a two-variable Taylor series for small a_R and a_I, one obtains

$$\tilde{h} = \hat{h}_0(x;b) + \hat{h}_1(x;b)a_R + \mathcal{O}(|a|^2),$$

where $\hat{h}_0 = \frac{1}{\Delta+\sqrt{\Delta^2-b^2x^2(1-x^2)}}$ and $\hat{h}_1 = \frac{bx(1-x^2)\hat{h}_0^2}{\sqrt{\Delta^2-b^2x^2(1-x^2)}}$. As $|a| \to 0$, linearizing Eq. (14) yields

$$a = \frac{\kappa_1 e^{i\beta}}{2}\langle(1-x^2)(a\hat{h}_0 + a_R bx\hat{h}_1)\rangle, \tag{26a}$$

$$1 = \frac{3\kappa_2 e^{i\beta}}{2}\langle x^2(1-x^2)\hat{h}_0\rangle. \tag{26b}$$

Equation (26b) is equivalent to Eq. (20), which gives solutions $\hat{b}$ and $\hat{\Delta}$ for the striped spiral chimera state. Equation (26a) can be written by

$$\begin{pmatrix} \hat{\mu}_R - \frac{\kappa_2}{\kappa_1} & -\hat{\nu}_I \\ \hat{\mu}_I & \hat{\nu}_R - \frac{\kappa_2}{\kappa_1} \end{pmatrix}\begin{pmatrix} a_R \\ a_I \end{pmatrix} = 0, \tag{27}$$

where $\hat{\mu} = (C-D)e^{i\beta}/2$ and $\hat{\nu} = De^{i\beta}/2$ with $C = \langle(1-x^2)/\sqrt{\hat{\Delta}^2 - \hat{b}^2x^2(1-x^2)}\rangle$ and $D = \langle(1-x^2)/[\hat{\Delta} + \sqrt{\hat{\Delta}^2 - \hat{b}^2x^2(1-x^2)}]\rangle$. We note that $\hat{\mu}$ and $\hat{\nu}$ depend only on the parameter α.

Applying again the implicit function theorem to Eq. (27), we obtain the bifurcation condition for the transition to the asymmetric striped spiral chimera as follows:

$$\kappa = f_2(\alpha) \equiv \tfrac{1}{2}\big[(\hat{\mu}+\hat{\nu})_R - \sqrt{(\hat{\mu}-\hat{\nu})_R^2 - 4\hat{\mu}_1\hat{\nu}_I}\big]. \tag{28}$$

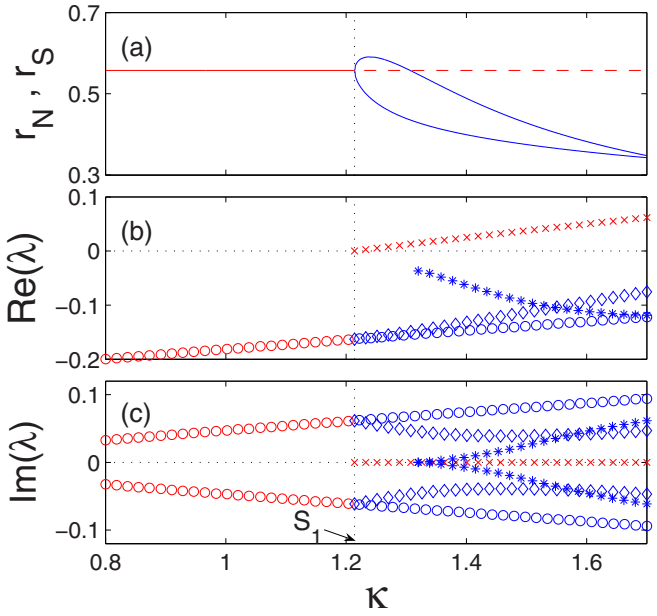

FIG. 8. Stability analysis of two-core spiral chimera states as $\kappa(\equiv\kappa_2)$ varies. Parameters: $\alpha = 0.7$ and $\kappa_1 = 1$, corresponding to the parameter values of Fig. 7(a). (a) Radii of the north and south cores versus κ, determined by Eq. (21). Solid and dashed curves represent the stable and unstable states, respectively. Panels (b) and (c) show the real and imaginary parts of the rightmost point spectrums, respectively, determined by Eq. (33). Red and blue symbols correspond to symmetric and asymmetric solution branches of panel (a), respectively. As κ increases past the symmetry-asymmetry boundary S_1, a positive real eigenvalue marked by red cross appears from zero eigenvalue embedded in the T-shaped essential spectrum, destabilizing the symmetric two-core spiral chimera. Meanwhile, a pair of complex conjugate eigenvalues with negative real part, marked by blue asterisks, pops out of the real part of the T-shaped essential spectrum.

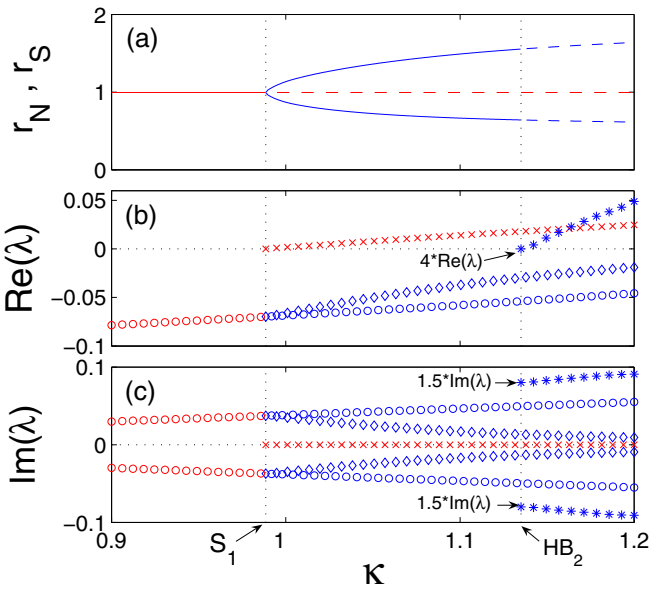

FIG. 9. Same picture as Fig. 8, but for $\alpha = 1.2$, corresponding to the parameter value of Fig. 7(b). The eigenvalues marked by crosses, circles, and diamonds exhibit the same mechanism underlying the supercritical symmetry-breaking bifurcation at the boundary S_1 as in Fig. 8. Beyond the critical value denoted by HB_2 with the increasing κ, a pair of complex conjugate eigenvalues, marked by asterisk and multiplied by constants, emerges from the imaginary axis of complex λ plane and moves into the half plane, destabilizing the asymmetric two-core spiral chimera state. Such Hopf-like bifurcation specifies the stability boundary HB_2 in Fig. 1.

Equation (28) gives the bifurcation boundary S_2 in Fig. 1, where the transition from the symmetric striped chimera to the asymmetric one occurs. We can see that $\kappa = 1$ for $\alpha = 0$ and $\kappa = \sqrt{2}$ for $\alpha = \frac{\pi}{2}$.

IV. STABILITY ANALYSIS

Substituting the ansatz $z(\mathbf{r},t) = z_0(\mathbf{r}) + \xi(\mathbf{r},t)$ with a small perturbation ξ into Eq. (6) and linearizing the result with respect to ξ, we have the perturbative equation

$$\frac{\partial\xi(\mathbf{r},t)}{\partial t} = \eta(\mathbf{r})\xi + \frac{1}{2}\left[\mathcal{G}\xi - z_0^2(\mathbf{r})(\mathcal{G}\xi)^*\right], \tag{29}$$

where $\eta(\mathbf{r}) = i\Delta - z_0(\mathbf{r})Z^*(\mathbf{r})$ and $\mathcal{G}$ denotes a convolution operator defined by

$$(\mathcal{G}v)(\mathbf{r},t) = e^{-i\alpha}\int_{\mathbb{S}^2} G(\mathbf{r},\mathbf{r}')v(\mathbf{r}',t)d\mathbf{r}'.$$

Using the expression (7), η can be written as

$$\eta(\mathbf{r}) = i\sqrt{\Delta^2 - R(\mathbf{r})^2}.$$

Equation (29) and its complex conjugate counterpart form a closed system for the linear stability analysis, of which the right-hand side defines a linear operator $\mathcal{L}$:

$$\frac{\partial}{\partial t}\mathbf{p} = \mathcal{L}\mathbf{p}, \tag{30}$$

where $\mathbf{p} = (\xi, \xi^*)^T$.

In general, for the finite-rank coupling function given by Eq. (2), the perturbative Eq. (30) has separable kernels and the linear stability analysis of all states can be performed [26–28,34].

The spectrums of the operator $\mathcal{L}$ consists of two parts: essential spectrum λ_{ess} and point spectrum λ_{pt}. The essential spectrum λ_{ess} is known explicitly by

$$\lambda_{\text{ess}} = \eta(\mathbf{r}) \text{ and } \lambda_{\text{ess}} = \eta^*(\mathbf{r}).$$

Therefore, the essential spectrums are determined for the coherent domain by

$$\lambda_{\text{ess}}^{\text{coh}} = -\sqrt{R^2(\mathbf{r}) - \Delta^2}, \tag{31}$$

and for the incoherent domain by

$$\lambda_{\text{ess}}^{\text{incoh}} = \pm i\sqrt{\Delta^2 - R^2(\mathbf{r})}. \tag{32}$$

Thus the spiral wave chimera state has a neutrally stable essential spectrum with a T-shaped continuous curves that consist of two intervals along the negative real and pure imaginary axes, corresponding to the coherent and incoherent domains, respectively.

As discussed in the Appendix, for the two-rank coupling function (3), we obtain the characteristic equation for the point

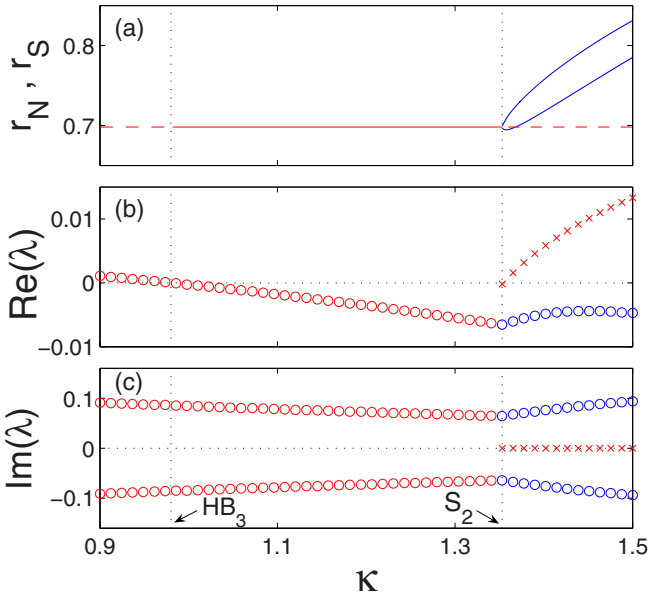

FIG. 10. Stability analysis of striped spiral chimera for $\alpha = 1.53$, $\kappa_1 = 1$ and varying $\kappa(\equiv \kappa_2)$, corresponding to Fig. 7(c). The format is the same as Figs. 8 and 9. With the increasing κ, a single, positive eigenvalue marked by (red) cross protrudes from the origin at the boundary S_2, presenting a supercritical symmetry-breaking bifurcation. This bifurcation specifies the stability boundary S_2 in Fig. 1. As κ decreases, two complex conjugate eigenvalues, marked by (red) open circles, simultaneously cross the imaginary axis into the right half of complex λ plane at a critical value marked by HB_3. Thus the symmetric striped spiral chimera undergoes a Hopf bifurcation, which determines the Hopf boundary HB_3 in Fig. 1.

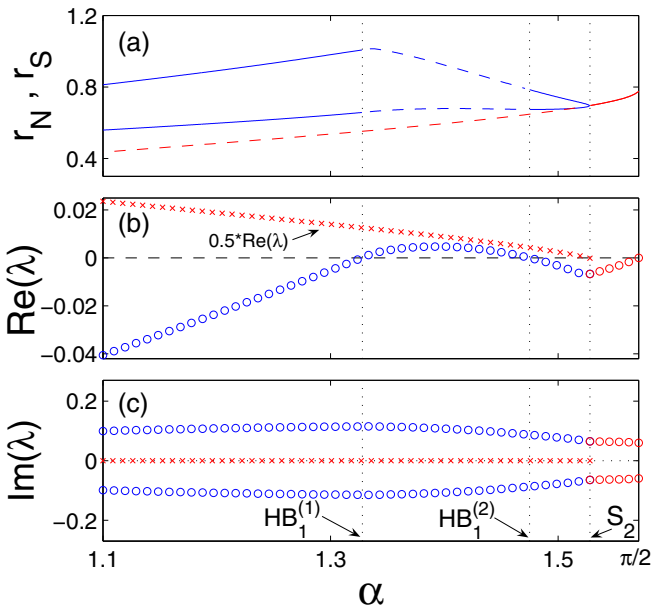

FIG. 11. Same picture as Fig. 10, but for fixed κ_2 with $\kappa_2 \equiv 1.35$ and instead varying α. As α decreases in panel (a) the asymmetric striped spiral chimera, marked by blue lines, bifurcates from the symmetric one, marked by red line, at the boundary S_2, where a positive eigenvalue marked by red cross (multiplied by 0.5) emerges from zero, as observed in panels (b) and (c). A pair of complex conjugate eigenvalues marked by blue open circles goes into the right half of complex λ plane at $HB_1^{(2)}$ and goes back into the left half at $HB_1^{(1)}$, giving rise to destabilization and successive stabilization of asymmetric spiral chimera states via the Hopf and inverse Hopf bifurcations, respectively. These two Hopf bifurcations occur on the single bent boundary HB_1 shown in Fig. 1.

spectrum $\lambda_{\rm pt}$ of $\mathcal{L}$ as follows:

$$\det\left[B(\lambda) - \mathbf{I}\right] = 0, \tag{33}$$

where B denotes 16×16 matrix defined by Eq. (A5) (see the Appendix for details).

The point spectrums satisfying Eq. (33) consists of a finite number of eigenvalues that are either real or appear as complex-conjugate pairs. It is typical of the chimera states that some of the point spectrums could emerge from and be absorbed into the T-shaped essential spectrums described by Eqs. (31) and (32) when the parameter values change. In particular, the transition from the symmetric spiral chimera to the asymmetric one occurs via the typical symmetry-breaking scenarios: A real eigenvalue suddenly emerges from a zero eigenvalue embedded in the essential spectrum at the bifurcation point and moves into the right half of the complex λ plane. Below we investigate the movement of the point spectrums $\lambda_{\rm pt}$ around the representative bifurcation boundaries shown in Fig. 1.

A. Destabilization of symmetric two-core spiral chimera states

Solving Eq. (33) numerically, we determine the point spectrums for both the symmetric and asymmetric two-core spiral chimera states described by Eqs. (15) and (13), respectively.

Figure 8 shows a typical result of numerically continuing the solutions of Eq. (33) as κ_2 is varied for $\kappa_1 = 1$ and $\alpha = 0.7$. These parameter values correspond to Fig. 7(a), which is again depicted in Fig. 8(a) for the sake of convenience. Figures 8(b) and 8(c) display the real and imaginary parts, respectively, of the rightmost point spectrums as a function of κ_2. The red and blue symbols correspond to the symmetric and asymmetric spiral chimera states, respectively.

As $\kappa(\equiv \kappa_2)$ increases, a pair of complex conjugate eigenvalues with negative real parts, marked by the red open circle, disappears at the point S_1 and instead real eigenvalues marked by red crosses emerge from the origin of the complex λ plane. This indicates that the symmetric two-core spiral chimera state becomes unstable when passing beyond the transition boundary S_1. On the other hand, the eigenvalues, marked by the blue open circles and diamonds, inherit from the red open circles corresponding to the symmetric chimera state have negative real parts. With the decreasing κ, a pair of complex conjugate eigenvalues, marked by the blue asterisk, collide on the real axis of the complex λ plane and then are absorbed in the T-shaped essential spectrums given by Eq. (31). Thus the generated asymmetric two-core spiral chimeras are stable.

Figure 9 depicts the same picture as Fig. 8 but for $\alpha = 1.2$, corresponding to the parameter set in Fig. 7(b). We can see that as the parameter κ increases the point spectrums determined by Eq. (33) represents the same behavior as that shown in Fig. 8, except for one aspect: As the parameter κ approaches the value denoted by HB_2, a pair of complex

conjugate eigenvalues marked by the (blue) asterisk protrudes from the imaginary part of the T-shaped essential spectrums given by Eq. (32) and they move further into the right half of the complex λ plane. In Figs. 9(b) and 9(c), the protruding eigenvalues are clearly distinguished from others by multiplying them by constants. When a pair of unstable complex conjugate eigenvalues appears from the neutrally stable essential spectrum, we call the bifurcation scenario the Hopf-like bifurcation. Thus the asymmetric two-core spiral chimera state undergoes a destabilization via a Hopf-like bifurcation, which determines the stability boundary HB_2 in shown in Fig. 1.

B. Destabilization of symmetric striped spiral chimera

Substituting the solutions described by Eqs. (18) and (13) into the characteristic Eq. (33) and solving it numerically, we determine the point spectrums for the symmetric and asymmetric spiral chimera states of a stripe-core mixed form.

Figure 10 shows the stability analysis of the striped spiral chimera for the same parameter set as in Fig. 7(c). In Fig. 10(a), the incoherent core radii are plotted as a function of κ. Figures 10(b) and 10(c) show the real and imaginary parts of the rightmost point spectrums λ, where the red and blue symbols correspond to the symmetric and asymmetric solution branches, respectively.

As κ increases, a single, positive eigenvalue marked by the red cross symbol appears from the essential spectrum at the symmetry-asymmetry boundary S_2 and moves further to the right on the real axis. Meanwhile, a pair of complex conjugate eigenvalues marked by blue open circles inherits from those marked by red circles at the boundary S_2 and moves within the left half plane of complex λ. This means that the stable asymmetric stripe two-core chimera state is created via a supercritical symmetry-breaking bifurcation. On the other hand, with the decreasing κ, a pair of complex conjugate eigenvalues, marked by the red open circles, crosses into the right half of the complex λ plane at a critical point denoted by HB_3, which results in a destabilization of the symmetric striped spiral chimera via the Hopf bifurcation. Such Hopf bifurcation points specify the stability boundary HB_3 in Fig. 1.

Figure 11 depicts the eigenvalue analysis for the striped spiral chimera state when κ is fixed but α is varied. We can see from Figs. 11(b) and 11(c) that the transition from symmetric striped spiral chimera to the asymmetric one is realized in a similar way to that shown in Fig. 10: a positive eigenvalue (marked by the red cross) protrudes from zero at the boundary S_2 as α decreases. With the increasing α, the real parts of two complex conjugate eigenvalues marked by blue open circles become positive and then negative at the boundaries $HB_1^{(1)}$ and $HB_1^{(2)}$, respectively. These two Hopf bifurcations determine the bent, single Hopf boundary HB_1 shown in Fig. 1.

V. GENERAL COUPLING SCHEME

We extend the analysis for the occurrence of the asymmetric spiral chimera state, described in Sec. III, to the case of an arbitrary choice of coupling function.

A. Two symmetric solutions

We consider the general coupling functions given by Eq. (2) for even $K > 2$. Unlike the case of the two-rank coupling function (3), the self-consistency Eq. (8) does not allow for symmetric solutions in the form of a single spherical harmonic, such as Eqs. (15) and (18).

Instead, there are *two* forms of symmetric solutions for the coupling function G_K. They have the form as follows:

$$Z_1 = e^{i\phi} \sum_{k=0}^{K/2-1} a_{2k+1} P_{2k+1}^1(\cos\theta), \tag{34a}$$

$$Z_2 = e^{i\phi} \sum_{k=1}^{K/2} a_{2k} P_{2k}^1(\cos\theta). \tag{34b}$$

In fact, substituting the ansatz (34a) into Eq. (11) and taking into account that $P_{2k+1}^1(x)$ is even and $P_{2k}^1(x)$ is odd, we obtain $a_\ell = 0$ when ℓ is even. Hence, Eq. (34a) provides a symmetric solution of the self-consistency Eq. (8) when a_{2k+1} satisfies the following equation:

$$a_{2k+1} = \sigma_{2k+1} \sum_{n=0}^{K/2-1} a_{2n+1} \langle h_1 P_{2n+1}^1(x) P_{2k+1}^1(x) \rangle, \tag{35}$$

where $\sigma_{2k+1} = \frac{\kappa_{2k+1} e^{i\beta}}{2(k+1)(2k+1)}$ and $h_1 = \frac{1}{\Delta + \sqrt{\Delta^2 - |Z_1|^2}}$.

The same is true for the ansatz (34b). Substituting the ansatz into Eq. (11) yields $a_\ell = 0$ for odd ℓ and thus Eq. (34b) gives another symmetric solution of Eq. (8), where a_{2k} for every $k \in \mathbb{Z}$ is the root of the following equations:

$$a_{2k} = \sigma_{2k} \sum_{n=1}^{K/2} a_{2n} \langle h_2 P_{2n}^1(x) P_{2k}^1(x) \rangle, \tag{36}$$

where $\sigma_{2k} = \frac{\kappa_{2k} e^{i\beta}}{2k(2k+1)}$ and $h_2 = \frac{1}{\Delta + \sqrt{\Delta^2 - |Z_2|^2}}$.

By using the property of the associated Legendre functions $P_n^1(x) = (1-x^2)^{1/2} \frac{d}{dx} P_n(x)$, Eq. (34) can be written by

$$Z_1 = \sin\theta e^{i\phi} \sum_{k=0}^{K/2-1} a_{2k+1} F_{2k+1}(\theta),$$

$$Z_2 = \sin\theta \cos\theta e^{i\phi} \sum_{k=1}^{K/2} a_{2k} F_{2k}(\theta),$$

where F_ℓ for $\ell \in \mathbb{Z}$ represents a polynomial with respect to $\cos^2\theta$. Therefore, by analogy with Eqs. (15) and (18), the spiral chimeras described by Eqs. (34a) and (34b) indicate the two-core and striped spiral chimeras, respectively, with reflection symmetry about the equator.

B. Onset of asymmetric spiral chimeras

When both a_{2k+1} and a_{2k} are nonzero solutions of Eq. (12), the order parameter given by Eq. (10) describes *asymmetric* spiral chimera states, which can be written in the decomposed form

$$Z = Z_1 + Z_2.$$

To seek the symmetry-breaking bifurcation around the symmetric solution Z_1, we represent Z_2 in the form $Z_2 =$

$\epsilon w(\theta)e^{i\phi}$ for small parameter $\epsilon \in \mathbb{R}$. Substituting

$$\hat{Z} = \hat{Z}_1 + \epsilon w$$

into $\tilde{h}$ in Eq. (12) and expanding it around $\hat{Z}_1$ in a two-variable Taylor series for small ϵw_R and ϵw_I, we obtain

$$\tilde{h} = h_1 + \epsilon(pw_R + qw_I) + \mathcal{O}(\epsilon^2), \tag{38}$$

where $p = \frac{h_1^2 \mathrm{Re}(\hat{Z}_1)}{\sqrt{\Delta^2 - |\hat{Z}_1|^2}}$ and $q = \frac{h_1^2 \mathrm{Im}(\hat{Z}_1)}{\sqrt{\Delta^2 - |\hat{Z}_1|^2}}$. As $\epsilon \to 0$, Eq. (12) can be written as

$$a_{2k+1} = \sigma_{2k+1} \sum_{n=0}^{K/2-1} a_{2n+1} \langle h_1 P_{2n+1}^1 P_{2k+1}^1 \rangle, \tag{39a}$$

$$a_{2k} = \sigma_{2k} \sum_{n=1}^{K/2} \{ \langle h_1 P_{2n}^1 P_{2k}^1 \rangle a_{2n} + \langle p\hat{Z}_1 P_{2n}^1 P_{2k}^1 \rangle \mathrm{Re}(a_{2n}) + \langle q\hat{Z}_1 P_{2n}^1 P_{2k}^1 \rangle \mathrm{Im}(a_{2n}) \}. \tag{39b}$$

Note that Eq. (39a) coincides with Eq. (35). We rewrite the complex Eq. (38b) as a system for a two-component real vector-function $\mathbf{e}_k = [\mathrm{Re}(a_{2k}), \mathrm{Im}(a_{2k})]^T$ as follows:

$$\mathbf{e}_k = \kappa_{2k} \sum_{n=1}^{K/2} C_{kn} \mathbf{e}_n, \qquad k = 1, \ldots, K/2, \tag{40}$$

where C_{kn} is a real 2×2 matrix given by

$$C_{kn} = \begin{pmatrix} \mathrm{Re}(M_{kn}) & -\mathrm{Im}(N_{kn} + K_{kn}) \\ \mathrm{Im}(M_{kn}) & \mathrm{Re}(N_{kn} + K_{kn}) \end{pmatrix},$$

with $M_{kn} = \frac{e^{i\beta}}{2k(2k+1)} \langle (h_1 + p\hat{Z}_1) P_{2n}^1 P_{2k}^1 \rangle$, $N_{kn} = \frac{e^{i\beta}}{2k(2k+1)} \langle h_1 P_{2n}^1 P_{2k}^1 \rangle$, and $K_{kn} = \frac{-ie^{i\beta}}{2k(2k+1)} \langle q\hat{Z}_1 P_{2n}^1 P_{2k}^1 \rangle$.

According to the implicit function theorem, the existence of the asymmetric solution branch that bifurcates continuously from the symmetric solution requires that the determinant of the coefficient matrix in Eq. (40) vanishes:

$$\det(D - \mathbf{I}_K) = 0, \tag{41}$$

where $\mathbf{I}_K$ denotes the $K \times K$-dimensional identity matrix and the matrix D is given by

$$D = \begin{pmatrix} \kappa_2 C_{11} & \kappa_2 C_{12} & \cdots & \kappa_2 C_{1,K/2} \\ \kappa_4 C_{21} & \kappa_4 C_{22} & \cdots & \kappa_4 C_{2,K/2} \\ \vdots & \vdots & \ddots & \vdots \\ \kappa_K C_{K/2,1} & \kappa_K C_{K/2,2} & \cdots & \kappa_K C_{K/2,K/2} \end{pmatrix}.$$

We note that each matrix block C_{kn} is completely determined after solving Eq. (39a) for the symmetric solution Z_1 and then it depends on the parameter α and the coefficients κ_n with odd n.

Solving simultaneously Eqs. (39a) and (41), we can find such a critical relationship between the coefficients κ_ℓ that the asymmetric solution branch bifurcates off the symmetric one as follows:

$$f(\alpha, \kappa_1, \ldots, \kappa_K) = 0. \tag{42}$$

It is obvious that, for the case of $K = 2$, Eq. (41) reduces to Eq. (24) and Eq. (42) is expressed by Eq. (25).

C. Piecewise-constant coupling function

We illustrate the universal occurrence of the asymmetric spiral wave chimeras via the piecewise-constant coupling function given by

$$G_{\mathrm{pc}}(\mathbf{r}, \mathbf{r}') = \begin{cases} \frac{\delta_1}{4\pi} & \text{if} \quad 0 < \gamma(\mathbf{r}, \mathbf{r}') \leqslant \pi r, \\ \frac{\delta_2}{4\pi} & \text{if} \quad \pi r < \gamma(\mathbf{r}, \mathbf{r}') \leqslant \pi, \end{cases} \tag{43}$$

where $r \in (0, 1)$ is a radius parameter. The balancing condition $\int_{\mathbb{S}^2} G_{\mathrm{pc}}(\mathbf{r}, \mathbf{r}') d\mathbf{r}' = 0$ yields a relation expression between the parameters δ_1, δ_2, and r as follows:

$$\cos \pi r = \frac{\delta_1 + \delta_2}{\delta_1 - \delta_2}.$$

Note that we can set either δ_1 or δ_2 to be a constant by rescaling time in Eq. (1). Below we fix δ_2 to be $\delta_2 = -0.3$ and choose δ_1 as an independent control parameter governing the coupling function G_{pc}.

Via the direct numerical simulations of Eq. (1) with the piecewise-constant coupling function (43), we observe the stable asymmetric two-core spiral chimera states in a wide parameter region.

Figure 12(a) shows the numerically found stability diagram for different types of chimera states in the (α, δ_1) plane when $\delta_2 = -0.3$. We see that asymmetric two-core spiral chimeras occur in the parameter region located between those of symmetric spiral chimera and higher-order chimera exhibiting the complicated chimera patterns. The snapshot of a representative of asymmetric two-core spiral chimera is depicted in Fig. 12(b). In the white region of Fig. 12(a), labeled higher-order spiral chimera, complicated chimera patterns were observed.

To get further insight into the transition from symmetric spiral chimera to asymmetric one, we consider the finite-rank approximation obtained via truncating the Legendre series of the coupling function. For the coupling function G_{pc}, the coefficients of the Legendre expansion in Eq. (2) are given by

$$\kappa_1 = \tfrac{3}{4}(\delta_1 - \delta_2) \sin^2 \pi r, \tag{44a}$$

$$\kappa_2 = \tfrac{5}{4}(\delta_1 + \delta_2) \sin^2 \pi r, \tag{44b}$$

$$\kappa_3 = \tfrac{7}{16}(\delta_1 - \delta_2)(5\cos^2 \pi r - 1) \sin^2 \pi r, \tag{44c}$$

$$\kappa_4 = \tfrac{9}{16}(\delta_1 + \delta_2)(7\cos^2 \pi r - 3) \sin^2 \pi r, \ \ldots. \tag{44d}$$

For the two-rank approximation of the form

$$G_{\mathrm{pc}} \approx G_2 \equiv \frac{1}{4\pi}(\kappa_1 P_1 + \kappa_2 P_2),$$

the bifurcation condition giving rise to the asymmetric spiral chimera is determined by Eq. (25). Substituting Eqs. (44a) and (44b) into Eq. (25), we can obtain the transition point from the symmetric two-core spiral chimera to the asymmetric one in the (α, δ_1) parameter plane. In Fig. 12(a), the dash-dotted (red) line indicates the transition boundaries obtained by the two-rank approximation. We can see that the two-rank approximation already exhibits a good agreement with the result from direct numerical simulations of Eqs. (1) and (43).

Now we consider an improved approximation of the coupling scheme such that the coupling function contains *four*

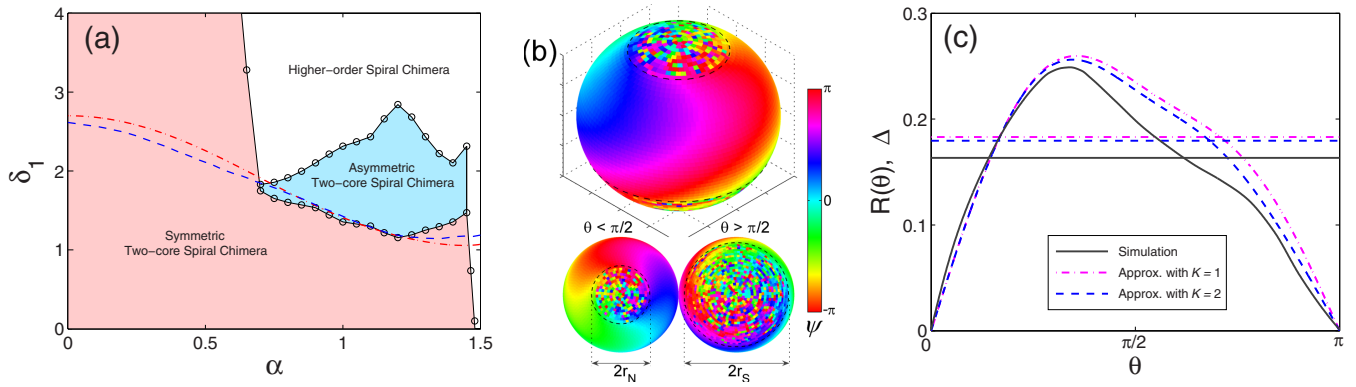

FIG. 12. Asymmetric spiral chimeras for the piecewise-constant coupling function (42). (a) Stability diagram in the (α, δ_1) parameter plane for $\delta_2 = -0.3$. Open circles indicate the stability boundaries, resulting from direct numerical simulations of Eqs. (1) and (42), where the solid lines are guides to the eye. Dash-dotted (red) and dashed (blue) lines denote theoretical predictions for the transition from the symmetric two-core spiral chimera to the asymmetric one, obtained by two-rank and four-rank approximations of coupling function, respectively. (b) Phase snapshot of asymmetric spiral chimera observed for parameter values $(\alpha, \delta_1) = (1, 1.9)$. (c) The longitudinal profile $R(\theta)$ and the Δ value for the chimera state shown in panel (b). Solid lines denote the simulation result, obtained from calculating Eq. (4) after numerically integrating Eqs. (1) and (42). Dash-dotted (red) and dashed (blue) lines correspond to theoretical results obtained by two- and four-rank approximations of the piecewise-constant coupling (42), respectively.

nonvanishing Legendre harmonics

$$G_{\rm pc} \approx G_4 \equiv \frac{1}{4\pi} \sum_{\ell=1}^{4} \kappa_\ell P_\ell .$$

The symmetric two-core spiral chimera is described by

$$Z_1 = \left[a_1 P_1^1(\cos\theta) + a_3 P_3^1(\cos\theta)\right] e^{i\phi},$$

for which Eq. (39a) can be written by

$$a_1 = \frac{\kappa_1 e^{i\beta}}{2} \left\langle P_1^1(x)\left[a_1 P_1^1(x) + a_3 P_3^1(x)\right] h_1 \right\rangle, \tag{45a}$$

$$a_3 = \frac{\kappa_3 e^{i\beta}}{12} \left\langle P_3^1(x)\left[a_1 P_1^1(x) + a_3 P_3^1(x)\right] h_1 \right\rangle. \tag{45b}$$

According to Eq. (41), the bifurcation condition for the asymmetric spiral chimera to occur is given by

$$\begin{vmatrix} \kappa_2 C_{11} - \mathbf{I}_2 & \kappa_2 C_{12} \\ \kappa_4 C_{21} & \kappa_4 C_{22} - \mathbf{I}_2 \end{vmatrix} = 0. \tag{46}$$

When replacing the values of κ_1, κ_2, κ_3, and κ_4 with those given by Eq. (44), the complex Eq. (45) and real Eq. (46) are equivalent to five real equations for the five real unknowns a_1, $\mathrm{Re}(a_3)$, $\mathrm{Im}(a_3)$, Δ, and δ_1.

We solved numerically Eqs. (45) and (46) to obtain δ_1 as a function of α, of which the result are depicted by the dashed (blue) line in Fig. 12(a). We can observe that the transition boundary to the asymmetric spiral chimera, obtained by four-rank approximation of $G_{\rm pc}$, is in better agreement a bit more with the result from the direct numerical simulations of Eqs. (1) and (43), as compared to the two-rank approximation.

Figure 12(c) shows the spatial profile $R(\theta)$ and Δ value for the asymmetric spiral chimera state shown in Fig. 12(b). The solid lines correspond to the result from direct numerical integration of Eqs. (1) and (43), where the order parameter was quantified by Eq. (4) and the Δ value was evaluated by the phase velocity of oscillators in the coherent domain. In Fig. 12(c), the dash-dotted and dashed lines indicate the theoretical results, obtained by solving Eq. (12) with two- and four-rank approximations $G_{\rm pc} \approx G_2$ and $G_{\rm pc} \approx G_4$, respectively.

VI. CONCLUSION

In summary, we have demonstrated the existence of asymmetric spiral chimera that consists of incoherent cores of different size on the spherical surface of nonlocally coupled identical oscillators. Such asymmetric spiral chimeras might be thought of as a genuine chimera state since under the influence of symmetric coupling scheme there occurs symmetry breaking in both aspects: The incoherent cores have different sizes as well as the coherent and incoherent domains coexist.

For the nonlocal coupling function with two harmonic modes, we have rigorously explored the bifurcation structure along the Ott-Antonsen invariant manifold to present a complete stability diagram for a variety of stationary spiral chimera patterns as well as a breathing asymmetric spiral chimera state. The conditions for the genesis of asymmetric spiral chimeras are derived, which reveals that the asymmetric spiral chimera state emerges via a supercritical symmetry-breaking bifurcation from the symmetric spiral chimera. For the general nonlocal coupling scheme, the asymmetric spiral chimeras occur in consequence of a competition between the odd and even modes of the Legendre expansion of the coupling function. Numerical simulations of the model system show good agreement with the theoretical results from the Ott-Antonsen ansatz equations.

We anticipate that the driving mechanism for the emergence of asymmetric spiral chimeras can be used and applied to search for asymmetric multicore spiral chimeras in experiments and realistic nature systems.

ACKNOWLEDGMENT

The authors thank Professor Hilda Cerdeira for a critical reading of the manuscript.

APPENDIX: DERIVATION OF CHARACTERISTIC EQUATION FOR THE POINT SPECTRUM

For the case of the coupling function with two Legendre harmonics given by Eq. (3), we substitute the ansatz

$$\begin{pmatrix} \xi(\mathbf{r},t) \\ \xi^*(\mathbf{r},t) \end{pmatrix} = \begin{pmatrix} q_1(\mathbf{r}) \\ q_2(\mathbf{r}) \end{pmatrix} e^{\lambda t}$$

into Eq. (30) to obtain

$$\lambda \mathbf{q}(\mathbf{r}) = J(\mathbf{r})\mathbf{q}(\mathbf{r}) + \sum_{\ell=1}^{2} \sum_{m=-\ell}^{\ell} Y_\ell^m(\mathbf{r}) Q_\ell(\mathbf{r}) \mathbf{c}_{\ell m}, \tag{A1}$$

where $\mathbf{q}(\mathbf{r}) = \binom{q_1(\mathbf{r})}{q_2(\mathbf{r})}$, $J(\mathbf{r}) = \begin{pmatrix} \eta(\mathbf{r}) & 0 \\ 0 & \eta^*(\mathbf{r}) \end{pmatrix}$, $Q_1(\mathbf{r}) = \frac{2\pi}{3}\kappa_1 Q(\mathbf{r})$, and $Q_2(\mathbf{r}) = \frac{2\pi}{5}\kappa_2 Q(\mathbf{r})$ with a matrix

$$Q(\mathbf{r}) = \begin{pmatrix} e^{-i\alpha} & -z_0^2(\mathbf{r}) e^{i\alpha} \\ -z_0^{*2}(\mathbf{r}) e^{-i\alpha} & e^{i\alpha} \end{pmatrix}.$$

The constant vectors $\mathbf{c}_{\ell m}$ are given by

$$\mathbf{c}_{\ell m} = \left\langle \left[Y_\ell^m(\mathbf{r})\right]^* \mathbf{q}(\mathbf{r}) \right\rangle_{\mathbb{S}^2}, \tag{A2}$$

where the angular bracket represents a spatial average over the surface of sphere: $\langle f(\mathbf{r})\rangle_{\mathbb{S}^2} \equiv \frac{1}{4\pi}\int_{\mathbb{S}^2} f(\mathbf{r}) d\mathbf{r} = \frac{1}{4\pi}\int_0^\pi \sin\theta \int_0^{2\pi} f(\mathbf{r}) d\phi d\theta$.

Assuming that $\det[\lambda I_2 - J(\mathbf{r})] \neq 0$, we solve Eq. (A1) for $\mathbf{q}(\mathbf{r})$ and substitute it into Eq. (A2) to obtain homogeneous equations for $\mathbf{c}_{\ell m}$ as

$$\mathbf{c}_{\ell m} = \sum_{k=1}^{2} \sum_{n=-k}^{k} \left\langle \left[Y_\ell^m(\mathbf{r})\right]^* Y_k^n(\mathbf{r}) E(\mathbf{r};\lambda) Q_k(\mathbf{r}) \right\rangle_{\mathbb{S}^2} \mathbf{c}_{kn}, \tag{A3}$$

where $E(\mathbf{r};\lambda) = [\lambda I_2 - J(\mathbf{r})]^{-1}$. Defining w_j and $\mathbf{c}_j$ as $(w_1,\ldots,w_8)^T := (Y_1^0, Y_1^1, Y_1^{-1}, Y_2^0, Y_2^1, Y_2^{-1}, Y_2^2, Y_2^{-2})^T$ and $(\mathbf{c}_1,\ldots,\mathbf{c}_8)^T := (\mathbf{c}_{10}, \mathbf{c}_{11}, \mathbf{c}_{1,-1}, \mathbf{c}_{20}, \mathbf{c}_{21}, \mathbf{c}_{2,-1}, \mathbf{c}_{22}, \mathbf{c}_{2,-2})^T$, Eq. (A3) can be rewritten by

$$\mathbf{c}_j = \sum_{k=1}^{8} B_{jk}(\lambda)\mathbf{c}_k, \quad \text{for} \quad j = 1,\ldots,8,$$

where B_{jk} is a two-dimensional matrix given by

$$B_{jk}(\lambda) = \begin{cases} \frac{2\pi}{3}\kappa_1 \left\langle w_j^*(\mathbf{r}) w_k(\mathbf{r}) E(\mathbf{r},\lambda) Q(\mathbf{r}) \right\rangle_{\mathbb{S}^2} \\ \qquad\qquad \text{for} \quad k = 1,2,3, \\ \frac{2\pi}{5}\kappa_2 \left\langle w_j^*(\mathbf{r}) w_k(\mathbf{r}) E(\mathbf{r},\lambda) Q(\mathbf{r}) \right\rangle_{\mathbb{S}^2} \\ \qquad\qquad \text{for} \quad k = 4,5,6,7,8. \end{cases} \tag{A4}$$

As a result, we obtain the characteristic equation for the point spectrums λ of $\mathcal{L}$ in the form of Eq. (33).

Each matrix block B_{jk} includes double integrals. For the spiral chimera states given by Eq. (13), however, the integrals with respect to the variable ϕ can be calculated, reducing the double integral calculations into simple integration with respect to θ, or equivalently, to $x \in [-1,1]$. Furthermore, employing the symmetries of the spiral chimera states given by Eq. (13), we can find that some of matrix blocks vanishes: $B_{12} = B_{13} = B_{15} = B_{16} = B_{21} = B_{27} = B_{28} = B_{31} = B_{37} = B_{38} = B_{42} = B_{43} = B_{45} = B_{46} = B_{51} = B_{54} = B_{57} = B_{58} = B_{61} = B_{64} = B_{67} = B_{68} = B_{72} = B_{73} = B_{75} = B_{76} = B_{78} = B_{82} = B_{83} = B_{85} = B_{86} = B_{87} = 0$. As a result, the matrix B can be written by

$$B = \begin{pmatrix} B_{11} & 0 & 0 & B_{14} & 0 & 0 & B_{17} & B_{18} \\ 0 & B_{22} & B_{23} & 0 & B_{25} & B_{26} & 0 & 0 \\ 0 & B_{32} & B_{33} & 0 & B_{35} & B_{36} & 0 & 0 \\ B_{41} & 0 & 0 & B_{44} & 0 & 0 & B_{47} & B_{48} \\ 0 & B_{52} & B_{53} & 0 & B_{55} & B_{56} & 0 & 0 \\ 0 & B_{62} & B_{63} & 0 & B_{65} & B_{66} & 0 & 0 \\ B_{71} & 0 & 0 & B_{74} & 0 & 0 & B_{77} & 0 \\ B_{81} & 0 & 0 & B_{84} & 0 & 0 & 0 & B_{88} \end{pmatrix}, \tag{A5}$$

where the nonvanishing matrix blocks are given as in the following:

$$B_{11} = \frac{\kappa_1}{2}\begin{pmatrix} e^{-i\alpha}\left\langle \frac{x^2}{\lambda-\eta}\right\rangle & 0 \\ 0 & e^{i\alpha}\left\langle \frac{x^2}{\lambda-\eta^*}\right\rangle \end{pmatrix},$$

$$B_{14} = \frac{\kappa_2\sqrt{15}}{20}\begin{pmatrix} e^{-i\alpha}\left\langle \frac{x(3x^2-1)}{\lambda-\eta}\right\rangle & 0 \\ 0 & e^{i\alpha}\left\langle \frac{x(3x^2-1)}{\lambda-\eta^*}\right\rangle \end{pmatrix},$$

$$B_{17} = \frac{3\kappa_2}{20}\sqrt{\frac{5}{2}}\begin{pmatrix} 0 & 0 \\ e^{-i\alpha}\left\langle \frac{x(1-x^2)h^{*2}\hat{Z}^{*2}}{\lambda-\eta^*}\right\rangle & 0 \end{pmatrix},$$

$$B_{18} = \frac{3\kappa_2}{20}\sqrt{\frac{5}{2}}\begin{pmatrix} 0 & e^{i\alpha}\left\langle \frac{x(1-x^2)h^2\hat{Z}^2}{\lambda-\eta}\right\rangle \\ 0 & 0 \end{pmatrix},$$

$$B_{22} = B_{33} = \frac{\kappa_1}{4}\begin{pmatrix} e^{-i\alpha}\left\langle \frac{1-x^2}{\lambda-\eta}\right\rangle & 0 \\ 0 & e^{i\alpha}\left\langle \frac{1-x^2}{\lambda-\eta^*}\right\rangle \end{pmatrix},$$

$$B_{23} = -\frac{\kappa_1}{4}\begin{pmatrix} 0 & e^{i\alpha}\left\langle \frac{(1-x^2)h^2\hat{Z}^2}{\lambda-\eta}\right\rangle \\ 0 & 0 \end{pmatrix},$$

$$B_{25} = \frac{3\sqrt{5}\kappa_2}{20}\begin{pmatrix} e^{-i\alpha}\left\langle \frac{x(1-x^2)}{\lambda-\eta}\right\rangle & 0 \\ 0 & e^{i\alpha}\left\langle \frac{x(1-x^2)}{\lambda-\eta^*}\right\rangle \end{pmatrix},$$

$$B_{26} = -\sqrt{2}B_{18},$$

$$B_{32} = -\frac{\kappa_1}{4}\begin{pmatrix} 0 & 0 \\ e^{-i\alpha}\left\langle \frac{(1-x^2)h^{*2}\hat{Z}^{*2}}{\lambda-\eta^*}\right\rangle & 0 \end{pmatrix},$$

$$B_{35} = -\sqrt{2}B_{17},$$

$$B_{44} = \frac{\kappa_2}{8}\begin{pmatrix} e^{-i\alpha}\left\langle \frac{(3x^2-1)^2}{\lambda-\eta}\right\rangle & 0 \\ 0 & e^{i\alpha}\left\langle \frac{(3x^2-1)^2}{\lambda-\eta^*}\right\rangle \end{pmatrix},$$

$$B_{47} = B_{84} = \sqrt{\frac{3}{2}}\frac{\kappa_2}{8}\begin{pmatrix} 0 & 0 \\ e^{-i\alpha\left\langle\frac{(3x^2-1)(1-x^2)h^{*2}\hat{Z}^{*2}}{\lambda-\eta^*}\right\rangle} & 0 \end{pmatrix},$$

$$B_{48} = B_{74} = \sqrt{\frac{3}{2}}\frac{\kappa_2}{8}\begin{pmatrix} 0 & e^{i\alpha\left\langle\frac{(3x^2-1)(1-x^2)h^2\hat{Z}^2}{\lambda-\eta}\right\rangle} \\ 0 & 0 \end{pmatrix},$$

$$B_{52} = B_{63} = \frac{5\kappa_1}{3\kappa_2}B_{25}, \quad B_{53} = \frac{5\kappa_1}{3\kappa_2}B_{26},$$

$$B_{55} = B_{66} = \frac{3\kappa_2}{4}\begin{pmatrix} e^{-i\alpha\left\langle\frac{x^2(1-x^2)}{\lambda-\eta}\right\rangle} & 0 \\ 0 & e^{i\alpha\left\langle\frac{x^2(1-x^2)}{\lambda-\eta^*}\right\rangle} \end{pmatrix},$$

$$B_{56} = -\frac{3\kappa_2}{4}\begin{pmatrix} 0 & e^{i\alpha\left\langle\frac{x^2(1-x^2)h^2\hat{Z}^2}{\lambda-\eta}\right\rangle} \\ 0 & 0 \end{pmatrix},$$

$$B_{62} = \frac{5\kappa_1}{3\kappa_2}B_{35}, \quad B_{71} = \frac{5\kappa_1}{3\kappa_2}B_{18}, \quad B_{81} = \frac{5\kappa_1}{3\kappa_2}B_{17},$$

$$B_{65} = -\frac{3\kappa_2}{4}\begin{pmatrix} 0 & 0 \\ e^{-i\alpha\left\langle\frac{x^2(1-x^2)h^{*2}\hat{Z}^{*2}}{\lambda-\eta^*}\right\rangle} & 0 \end{pmatrix},$$

$$B_{77} = B_{88} = \frac{3\kappa_2}{16}\begin{pmatrix} e^{-i\alpha\left\langle\frac{(1-x^2)^2}{\lambda-\eta}\right\rangle} & 0 \\ 0 & e^{i\alpha\left\langle\frac{(1-x^2)^2}{\lambda-\eta^*}\right\rangle} \end{pmatrix}.$$

For the asymmetric spiral chimera states given by $Z = (a + b\cos\theta)\sin\theta e^{i\phi}$, the functions $\hat{Z} = \hat{Z}(x)$, $\eta = \eta(x)$ and $h = h(x)$ are to be taken as in the following:

$$\hat{Z} = (a + bx)\sqrt{1 - x^2}, \quad \eta = i\sqrt{\Delta^2 - (1 - x^2)|a + bx|^2},$$
$$h = \frac{1}{\Delta + \sqrt{\Delta^2 - (1 - x^2)|a + bx|^2}}.$$

[1] A. Pikovsky, M. Rosenblum, and J. Kurths, *Synchronization: A Universal Concept in Nonlinear Sciences* (Cambridge University Press, Cambridge, England, 2001).

[2] S. H. Strogatz, *Sync: The Emerging Science of Spontaneous Order* (Hyperion, New York, 2003).

[3] Y. Kuramoto, *Chemical Oscillations, Waves, and Turbulence* (Springer, New York, 1984).

[4] J. A. Acebron, L. L. Bonilla, C. J. Perez Vicente, F. Ritort, and R. Spigler, The Kuramoto model: A simple paradigm for synchronization phenomena, Rev. Mod. Phys. **77**, 137 (2005).

[5] S. H. Strogatz, From Kuramoto to Crawford: Exploring the onset of synchronization in populations of coupled oscillators, Physica D **143**, 1 (2000).

[6] Y. Kuramoto and D. Battogtokh, Coexistence of Coherence and Incoherence in Nonlocally Coupled Phase Oscillators, Nonlinear Phenom. Complex Syst. **5**, 380 (2002).

[7] D. M. Abrams and S. H. Strogatz, Chimera States for Coupled Oscillators, Phys. Rev. Lett. **93**, 174102 (2004).

[8] A. E. Motter, Spontaneous synchrony breaking, Nat. Phys. **6**, 164 (2010).

[9] M. J. Panaggio and D. M. Abrams, Chimera states: Coexistence of coherence and incoherence in networks of coupled oscillators, Nonlinearity **28**, R67 (2015).

[10] E. Schöll, Synchronization patterns and chimera states in complex networks: Interplay of topology and dynamics, Eur. Phys. J.: Spec. Top. **225**, 891 (2016).

[11] O. E. Omel'chenko, The mathematics behind chimera states, Nonlinearity **31**, R121 (2018).

[12] S. Majhi, B. K. Bera, D. Ghosh, and M. Perc, Chimera states in neuronal networks: A review, Phys. Life Rev. **28**, 100 (2019).

[13] F. Parastesh, S. Jafari, H. Azarnoush, Z. Shahriari, Z. Wang, S. Boccaletti, and M. Perc, Chimeras, Phys. Rep. **898**, 1 (2021).

[14] Y. Kuramoto and S. Shima, Rotating Spirals without Phase Singularity in Reaction-Diffusion Systems, Prog. Theor. Phys. Suppl. **150**, 115 (2003).

[15] S. Shima and Y. Kuramoto, Rotating spiral waves with phase-randomized core in nonlocally coupled oscillators, Phys. Rev. E **69**, 036213 (2004).

[16] J. Davidsen, Symmetry-breaking spirals, Nat. Phys. **14**, 207 (2018).

[17] C. Laing, The dynamics of chimera states in heterogeneous Kuramoto networks, Physica D **238**, 1569 (2009).

[18] C. Gu, G. St-Yves, and J. Davidsen, Spiral Wave Chimeras in Complex Oscillatory and Chaotic Systems, Phys. Rev. Lett. **111**, 134101 (2013).

[19] E. A. Martens, C. Laing, and S. H. Strogatz, Solvable Model of Spiral Wave Chimeras, Phys. Rev. Lett. **104**, 044101 (2010).

[20] O. E. Omel'chenko, M. Wolfrum, S. Yanchuk, Y. L. Maistrenko, and O. Sudakov, Stationary patterns of coherence and incoherence in two-dimensional arrays of non-locally coupled phase oscillators, Phys. Rev. E **85**, 036210 (2012).

[21] J. Xie, E. Knobloch, and H.-C. Kao, Twisted chimera states and multicore spiral chimera states on a two-dimensional torus, Phys. Rev. E **92**, 042921 (2015).

[22] O. E. Omel'chenko, M. Wolfrum, and E. Knobloch, Stability of Spiral Chimera States on a Torus, SIAM J. Appl. Dyn. Syst. **17**, 97 (2018).

[23] M. Bataille-Gonzalez, M. G. Clerc, and O. Omel'chenko, Moving spiral wave chimeras, Phys. Rev. E **104**, L022203 (2021).

[24] M. J. Panaggio and D. H. Abrams, Chimera states on the surface of a sphere, Phys. Rev. E **91**, 022909 (2015).

[25] C. Laing, Chimeras in two-dimensional domains: Heterogeneity and the continuum limit, SIAM J. Appl. Dyn. Syst. **16**, 974 (2017).

[26] R.-S. Kim and C.-U. Choe, Symmetry-broken states on a spherical surface of coupled oscillators: From modulated coherence to spot and spiral chimeras, Phys. Rev. E **98**, 042207 (2018).

[27] R.-S. Kim, G.-H. Tae, and C.-U. Choe, Emergence of stripe-core mixed spiral chimera on a spherical surface of nonlocally coupled oscillators, Int. J. Bifurcation Chaos **31**, 2150182 (2021).

[28] C.-U. Choe, R.-S. Kim, and H. Jo, Spiral wave chimeras induced by heterogeneity in phase lags and time delays, Physica D **422**, 132892 (2021).

[29] J. F. Totz, J. Rode, M. R. Tinsley, K. Showalter, and H. Engel, Spiral wave chimera states in large populations of coupled chemical oscillators, Nat. Phys. **14**, 282 (2018).

[30] J. F. Totz, M. R. Tinsley, H. Engel, and K. Showalter, Transition from spiral wave chimeras to phase cluster states, Sci. Rep. **10**, 7821 (2020).

[31] E. Ott and T. M. Antonsen, Low dimensional behavior of large systems of globally coupled oscillators, Chaos **18**, 037113 (2008).

[32] E. Ott and T. M. Antonsen, Long time evolution of phase oscillator systems, Chaos **19**, 023117 (2009).

[33] G. D. Ermentrout and D. H. Terman, *Mathematical Foundations of Neuroscience* (Springer, Berlin, 2010).

[34] O. E. Omel'chenko, Coherence-incoherence patterns in a ring of non-locally coupled phase oscillators, Nonlinearity **26**, 2469 (2013).